Coherent pressure structures in turbulent channel flow

Filipe R. do Amaral [*]

*Département Fluides, Thermique, Combustion, Institut Pprime-CNRS-Université de
Poitiers-ENSMA, 86000 Poitiers, France*

André V. G. Cavalieri [†]

*Divisão de Engenharia Aeroespacial, Instituto Tecnológico de Aeronáutica,
12228-900 São José dos Campos, SP, Brazil*

Most of the studies on pressure fluctuations in wall-bounded turbulent flows aim at obtaining statistics as power spectra and scaling laws, especially at the walls. In the present study we study energetic coherent pressure structures of turbulent channel flows, aiming at a characterization of dominant coherent structures throughout the channel. Coherent structures are detected using spectral proper orthogonal decomposition (SPOD) and modeled using resolvent analysis, similarly to related works dealing with velocity fluctuations but this time using pressure fluctuations as the output of interest. The resolvent operator was considered with and without the Cess eddy-viscosity model. Direct numerical simulations (DNSs) of incompressible turbulent channel flows at friction Reynolds numbers of approximately 180 and 550 were employed as databases in this study. Three representative dominant structures emerged from a preliminary spectral analysis: near-wall, large-scale, and spanwise-coherent structures. For frequency–wave number combinations corresponding to these three representative structures, SPOD results show a strong dominance of the leading mode, highlighting low-rank behavior of pressure fluctuations. The leading resolvent mode closely agrees with the first SPOD mode, providing support to studies that showed better performance of resolvent-based estimators when predicting pressure fluctuations compared to velocity fluctuations [Amaral *et al.*, J. Fluid Mech. **927**, A17 (2021)]. The dominant mechanisms of the analyzed modes are seen to be the generation of quasistreamwise vortices with pressure fluctuations appearing close to vortex centers. A study on the individual contributions of the nonlinear terms (treated as forcing in resolvent analysis) to the pressure output reveals that each forcing component plays a constructive role to the input-output formulation, which also helps understanding the weaker role of forcing "color" in driving pressure fluctuations.

I. INTRODUCTION

The understanding of pressure fluctuations in wall-bounded turbulent flows is of fundamental importance for many practical applications such as sound radiation and structural vibration. With the world community appeal for "greener by design" vehicles and technologies, lower sound emission is one of the goals that have been pursued towards diminishing environmental pollution, as noise is also a concern regarding human and wildlife health issues. On the other hand, fluid-structure

---

[*]Contact author: filipe.ramos.do.amaral@univ-poitiers.fr

[†]Contact author: andre@ita.br

interactions are of concern for structural integrity. Moreover, pressure fluctuations on the surface of a sharp body, such as the trailing-edge of a wing, scatters sound that is propagated to the far field and may also induce structural vibrations. Besides aircraft wings, this is especially important for wind turbines, fans, and propellers [1].

Although the past few decades have experienced great advances in both computations and experiments of wall turbulence, the study of pressure fluctuations in wall-bounded turbulent flows has received less attention than the analysis of velocity fluctuations. On the experimental side, most of the studies were focused on the analysis of wall-pressure measurements [2–5], with the microphones usually mounted in arrays flush to the test model wall [6]. Such arrays have limited aperture and a finite number of sensors, which, among other issues, limits the measurement resolution. Test facilities also suffer from background noise that can contaminate the measurements [7], especially at low Reynolds numbers [8]. The small scales associated with the turbulent flow also impose a challenge to reliable measurement of pressure fluctuations [9]. Hence, they are an important part of the literature regarding such topic relies on theoretical and numerical studies.

High-fidelity numerical simulations have the advantage of obtaining the entire flow field, not necessarily limited to the channel walls. For instance, Kim *et al.* [10] conducted a direct numerical simulation (DNS) of a channel flow with friction Reynolds number (Re_τ) of 180. Their database was further used by Choi and Moin [11], who computed the wall-pressure spectra. When comparing their frequency spectra with experimental data at different Reynolds numbers, the authors obtained different scaling laws for the low- and high-frequency ranges. The lower frequencies better collapsed with outer variables, whereas inner variables better fitted the higher frequencies. This result agrees with the experimental data by Farabee and Casarella [4], who studied wall-pressure fluctuations in boundary layers. Choi and Moin [11] also identified a small region with a -5 power-law decay rate for both frequency and streamwise wave-number spectra, i.e., for $\omega \nu / u_\tau^2 > 1$, where ω is the angular frequency, ν is the fluid kinematic viscosity, and u_τ is the friction velocity, and for $\alpha^+ = \alpha \nu / u_\tau > 0.1$, where α is the streamwise wave number. Such decay rate was also found in later studies [12–14]. For even higher frequencies, the spectra decay at higher rates. Another observation by Choi and Moin [11] regards the effect of the Reynolds number on the wall-pressure spectra. Increasing the Reynolds number leads to increased power at the high-frequency band when outer scaling is considered, whereas the low-frequency band increases the power with Reynolds number for inner scaling.

Kim [15] also explored the $\mathrm{Re}_\tau = 180$ database by Kim *et al.* [10], focusing on the pressure fluctuations. The author decomposed the pressure fluctuations into rapid (linear) and slow (nonlinear) components, where the distinction between such components relies on the linear and nonlinear interactions present in the Poisson equation for pressure. The rapid part of pressure fluctuations, which contains the mean velocity gradient, responds immediately to any change imposed to the flow field, whereas the slow part reacts through nonlinear interactions. The results obtained by Kim [15] show that the slow component is dominant over the rapid component, i.e., the nonlinear source terms in the Poisson equation play a major role in the pressure fluctuations behavior. Another relevant finding by the author was obtained through the modeling of the wall fluctuations by a Green's function, where the pressure was written as a convolution of a Green's function with a source term. He showed the instantaneous pressure at one of the channel walls is affected by source terms that are present at the opposite wall, highlighting that pressure fluctuations comprise large spatial scales and have a nonlocal nature.

Regarding the power spectra of wall pressure and shear stress, Hu *et al.* [12] conducted a series of numerical simulations for channel flows up to $\mathrm{Re}_\tau = 1440$. The authors compared their results with spectra of channel, pipe, and boundary-layer flows at several Reynolds numbers. The wall-pressure spectrum showed a reasonable collapse for $\mathrm{Re}_\tau \geqslant 360$, with inner scaling for the higher frequencies and outer scaling for the lower frequencies, as previously observed by Choi and Moin [11]. The premultiplied frequency spectra exhibited a peak at $\omega^+ \approx 0.3$. This peak frequency is in agreement with the results obtained by Anantharamu and Mahesh [13], which conducted DNS of channel flow at $\mathrm{Re}_\tau = 180$ and 400 aiming at exploring the source of wall-pressure fluctuations. Anantharamu and

Mahesh [13] also found that the wall-pressure fluctuation peak for the premultiplied wave-number spectra corresponds to a streamwise wavelength $\lambda_x^+ \approx 200$, where $\lambda_x^+ = 2\pi/\alpha^+$, for fluctuations in the buffer layer for $y^+ \approx 15$, where y^+ is the wall-normal coordinate in inner (wall or viscous) units and α^+ is the streamwise wave number in inner units. A pressure premultiplied spectrum peak in the range $\lambda_x^+ \approx 200$ to 300 was also reported by Panton *et al.* [16], who studied several DNS databases of channel flow for Re_τ up to 5186 and zero pressure gradient boundary-layer flows for Re_τ up to 1271. In addition, Panton *et al.* [16] proposed scaling laws for the pressure statistics at the wall and inner and outer layers.

In recent years there has been substantial effort in modeling coherent structures in wall turbulence [17–19]. Efforts towards this direction include the study of linearized models and modal decomposition of databases [20–22]. For linearized models, the problem is written in the input-output format in the frequency domain and the nonlinear terms of the Navier-Stokes (N-S) system are treated as an external forcing that generates a response through the resolvent operator, obtained by inversion of the linearized N-S (LNS) operator considering the mean profile as a base flow [23,24]. The inputs correspond to the forcing terms (nonlinear terms of N-S system), whereas the outputs denote the flow state (e.g., velocity and pressure components). In the frequency domain, the input and outputs are written as two-point space-time statistics, i.e., cross-spectral densities (CSDs), and can be accurately computed directly from, e.g., snapshots of DNS data. Resolvent analysis permits the elucidation of the role played by the nonlinear terms of the N-S system. Application of singular value decomposition (SVD) on the resolvent operator provides the most amplified forcing and response modes. Resolvent modes also display a hierarchical character, ranked from high to low gain. It should be emphasized that in order to obtain the resolvent operator, hence the resolvent modes, only the mean flow and the boundary conditions are needed. As the resolvent analysis employs a linearization over a mean flow, it may reveal the dominant amplification mechanisms. This is in contrast with the use of the Poisson equation for pressure fluctuations, where no assumption is made about the base flow, and a normal linear operator (the Laplacian) does not display gain separations as significant as the ones obtained with the LNS. For instance, Luhar *et al.* [25] used resolvent analysis to explore wall-pressure fluctuations in turbulent pipe flow obtained through DNS and verified that the rank-1 (optimal) response mode contains most of the relevant features present in the DNS. They also show the pressure fluctuations that can be identified through the resolvent analysis are related to the rapid (linear) pressure component. The slow (nonlinear) pressure component, on the other hand, needs the solution of the full nonlinear turbulence field, since it is related to the divergence of the full forcing field.

Response modes obtained from resolvent analysis may be compared to appropriate modal decompositions of data, and a suitable approach is spectral proper orthogonal decomposition (SPOD). SPOD extracts a set of orthogonal modes from flow realizations in frequency domain that are optimal according to an appropriate inner product [26,27]. The modes are ranked according to their energetic content, i.e., the first mode is the most energetic one and the subsequent modes contain less energy than the previous mode. The resolvent or response modes are equivalent to the SPOD modes when the flow is forced by stochastic white noise [26,28,29]. Moreover, if the resolvent has a large gain separation, i.e., $\sigma_1 \gg \sigma_{2,3,\ldots,n}$, then the optimal flow response is expected to be dominant and is thus similar to the most energetic SPOD mode. In this case, even a white-noise assumption for the forcing terms in the resolvent framework leads to reasonable agreement between SPOD and resolvent analysis. Therefore, the resolvent analysis becomes a powerful method to predict dominant coherent structures in turbulent flows.

SPOD and resolvent analysis applied to study coherent structures in wall-bounded flows normally focus on the velocity components. Early works by McKeon and Sharma [23] and Hwang and Cossu [24] investigated pipe and channel flows, respectively, for a wide range of Reynolds numbers using resolvent analysis to study the most amplified velocity responses. In the channel flow problem studied by Hwang and Cossu [24], the authors showed the most amplified structures are streamwise streaks which are forced by streamwise vortices. Streaks are coherent structures, usually identified in the near-wall region of wall-bounded turbulent flows and can be pictured as spanwise aligned layers

of low- and high-speed streamwise velocity flow driven by quasistreamwise vortices that organize the momentum transfer and energy dissipation, redistributing the kinetic energy [30,31]. Abreu *et al.* [32] studied DNS channel flow databases at $Re_\tau \approx 180$ and 550 and employed SPOD and resolvent analysis to identify and model near-wall coherent structures for several combinations of wave numbers and frequencies, with only velocity state components considered in the study. They verified that streaks and streamwise vortices were the most energetic structures in the near-wall region, as expected from the literature of wall-bounded turbulent flows [31]. The leading SPOD and resolvent modes were in close agreement when the lift up mechanism [33,34] was active, similarly to what was found in a related turbulent pipe flow study [35]. Lift up is a linear mechanism that amplifies finite amplitude streamwise fluctuations in shear flows through the action of vertical fluctuations, hence moving low-speed flow from the walls upwards [36,37].

The resolvent operator can be written to include an eddy-viscosity model (which substitutes the constant molecular viscosity) to mimic a portion of the nonlinear terms of the N-S system [22,24]. In this approach, the nonlinear forcing statistics are still modeled as white noise but the linear operator is modified by the inclusion of the eddy-viscosity model, the most common model being the one proposed by Cess [38]. Eddy-viscosity approaches were successfully employed, e.g., to compute optimal temporal transient growths supported in turbulent channel flow [39,40], optimally amplified streaks [41], to introduce optimal perturbations (streaks) in confined turbulent flows [42], among others. Symon *et al.* [19] and Symon *et al.* [43] observed the use of a Cess eddy-viscosity model was helpful in the resolvent analysis in channel flows, improving the resolvent modes capacity to predict the most energetic structure (streamwise streaks). However, the use of a singe eddy-viscosity profile does not lead to accurate predictions at all scales.

The work by byMorra *et al.* [44] employed SPOD and resolvent analysis to investigate turbulent channel flow at $Re_\tau \approx 180$ and 550 obtained through DNS. The authors focused on extracting the nonlinear forcing terms from the database in order to show how such terms affect the resolvent outputs. In their study, the power spectral density (PSD) of the state (velocity fluctuation) components, evaluated through the input-output formulation for different forcing statistics (input) models, where compared with the true state components, obtained directly from the DNS, for the most energetic near-wall and large-scale structures. They showed that a rank-2 approximation of the forcing, containing only the two most energetic SPOD modes, is a sufficient approximation of the nonlinear terms, leading to a response with reasonable accuracy when comparing with DNS data. The performance of the Cess eddy-viscosity-modeled forcing on the accuracy of resolvent analysis was also explored and the authors verified the use of the eddy-viscosity model boosted the accuracy of the predictions of the output (response) in comparison to the resolvent operator using only the molecular viscosity.

The present study explores the DNS databases of turbulent channel flow at $Re_\tau \approx 180$ and 550. Such DNS databases were validated against established results in the literature. The aim is to investigate coherent pressure fluctuations in channel flows using SPOD and resolvent analysis. The coherent structures were obtained through the analysis of the pressure spectra at $y/H = 0$ (corresponding to the channel wall) and $y/H = 0.5$, where H is the channel half-height, targeting the most energetic structures. Such wall-normal distances were selected as representative locations of near-wall and large-scale structures in wall-bounded flows. The resolvent operator is studied with and without the inclusion of the Cess eddy-viscosity model Cess [38]. We examine the accuracy of input-output analysis to predict pressure fluctuations and the role of nonlinear forcing statistics in constructing the flow response in order to provide knowledge on the dynamics of pressure structures in wall turbulence. Low-rank models for the forcing component and their effect on the pressure component estimate is also addressed.

The remainder of this paper is organized as follows. After this introduction, Sec. II addresses the methodology, including the description of the physical problem, the tools employed to analyze the data (resolvent analysis or input-output formulation, two-point statistics, and SPOD), and details of the DNS databases. The energy spectra as a function of the streamwise and spanwise wave numbers, as well as the frequency, for wall-normal distances corresponding to the near-wall and

large-scale structures are reported in Sec. III. Comparisons between SPOD and resolvent modes, with and without the inclusion of the Cess eddy-viscosity model on the linear operator are discussed in Sec. IV. In Sec. V we employ the input-output formulation to elucidated the role of the forcing terms through the study of the effect of each forcing component (input) on the pressure component (output). Finally, Sec. VI summarizes the conclusions.

II. METHODOLOGY

A. Governing equations

The flow is governed by the incompressible Navier-Stokes system in the absence of external body forces. The vector of velocity components is given by $\boldsymbol{u} = [u_x \, u_y \, u_z]$, with u_x, u_y, and u_z as the streamwise, wall-normal, and spanwise velocity components, respectively. The full state vector is written as

$$\boldsymbol{q} = [\boldsymbol{u} \, p]^T, \tag{1}$$

with $\boldsymbol{q} = \boldsymbol{q}(x, y, z, t)$, where x, y, and z indicate the streamwise, wall-normal, and spanwise directions, respectively; t denotes time; p is the pressure component; and T denotes transpose operator. A Reynolds decomposition was employed over the flow state components, i.e., $\boldsymbol{q} = \bar{\boldsymbol{q}} + \boldsymbol{q}'$, where $\bar{\boldsymbol{q}}$ is the mean flow and $\boldsymbol{q}'$ is the fluctuation.

In the present study, the mean flow at the streamwise direction is employed to construct the linearized Navier-Stokes system, e.g., $\bar{\boldsymbol{q}} = [\bar{U}(y) \, z \, z \, z]^T$, where z is the zeros vector and $\bar{U}(y)$ is the mean flow velocity profile. The mean pressure gradient that drives the channel flow has no contribution for the linearised Navier-Stokes system for nonzero frequency and wave number, as discussed by Morra *et al.* [44], and hence is not considered here. Following Morra *et al.* [44] and dropping the primes from the fluctuation quantities to simplify notations, the Reynolds-decomposed N-S system is given by

$$\partial_t \boldsymbol{u} + (\boldsymbol{u} \cdot \nabla)\bar{U} + (\bar{U} \cdot \nabla)\boldsymbol{u} + \nabla p - \frac{1}{\text{Re}_\tau}\nabla^2 \boldsymbol{u} = \boldsymbol{f}, \tag{2a}$$

$$\nabla \cdot \boldsymbol{u} = 0, \tag{2b}$$

where ∂_t denotes partial derivative with respect to time t, ∇ is the gradient operator, and ∇^2 is the Laplacian operator. The nonlinear terms of the N-S system, i.e.,

$$\boldsymbol{f} = -(\boldsymbol{u} \cdot \nabla)\boldsymbol{u} + \overline{(\boldsymbol{u} \cdot \nabla)\boldsymbol{u}}, \tag{3}$$

are interpreted as external forcing [23] and, in Cartesian coordinates, are given by the vector $\boldsymbol{f} = [f_x \, f_y \, f_z]^T$, where f_x, f_y, and f_z are the streamwise, wall-normal, and spanwise forcing components, respectively. The friction Reynolds number is defined as $\text{Re}_\tau = u_\tau H/\nu$. The Reynolds number may also be given in terms of the bulk velocity U_b, i.e., $\text{Re} = U_b H/\nu$.

B. Resolvent analysis and input-output formulation

Resolvent analysis is a technique in which the governing equations are linearized over a base flow and written in the input-output format. The inputs refer to the forcing terms and the outputs are the flow responses [23,24,45]. The LNS operator includes the base flow and adequate boundary conditions, e.g., no-slip conditions at the top and bottom walls for channel flows.

For a discrete domain, one has

$$\boldsymbol{M}\frac{d\boldsymbol{q}(t)}{dt} = \boldsymbol{A}\boldsymbol{q}(t) + \boldsymbol{B}\boldsymbol{f}, \tag{4a}$$

$$\boldsymbol{y}(t) = \boldsymbol{C}\boldsymbol{q}(t), \tag{4b}$$

where $\boldsymbol{M}$ is a diagonal matrix whose entries are set to 1 and zero for the momentum and continuity equations, respectively, $\boldsymbol{A}$ is the linear operator, assumed as stable, $\boldsymbol{B}$ is the input matrix that restricts

the forcing terms to appear only in the momentum equation, and C is a matrix that selects a relevant output y. Throughout this study, C restricts the observations to the components of the state related to pressure fluctuations, unless otherwise specified. Expression (4b) is exact provided that the forcing terms are computed from the same DNS database employed to obtain the state components.

Equation (4b) can be written in frequency and wave-number domains as

$$\hat{y}(\omega) = \{C[-i\omega M - A(\omega)]^{-1}B\}\hat{f}(\omega), \tag{5}$$

where dependencies on streamwise and spanwise wave numbers α and β, respectively, and wall-normal distance y, were dropped to simplify notations. Moreover,

$$\hat{y}(\omega) = \int_{-\infty}^{\infty} y(t)e^{i\omega t} dt \tag{6}$$

is the Fourier transform of y, with analogous expression for other variables. Hats indicate variables in the frequency domain, ω is the temporal frequency, and $i = \sqrt{-1}$.

In expression (5), between brackets one has $H = CRB$, where $R = L^{-1}$ and $L = (-i\omega M - A)$. L is the LNS operator, whereas R denotes the resolvent operator and H is the resolvent operator including, through operators C and B, the observation and forcing restrictions, respectively.

Following McKeon [22], the LNS operator is written as

$$L = \begin{bmatrix} i\alpha\bar{U} - i\omega I - \frac{1}{\text{Re}}\nabla^2 & \frac{d\bar{U}}{dy} & Z & i\alpha I \\ Z & i\alpha\bar{U} - i\omega I - \frac{1}{\text{Re}}\nabla^2 & Z & \frac{d}{dy} \\ Z & Z & i\alpha\bar{U} - i\omega I - \frac{1}{\text{Re}}\nabla^2 & i\beta I \\ i\alpha I & \frac{d}{dy} & i\beta I & Z \end{bmatrix}, \tag{7}$$

for a triplet (α, β, ω). Here $\bar{U}$ is the mean turbulent streamwise velocity profile, $\nabla^2 = (\frac{d^2}{dy^2} - k^2 I)$ with $k^2 = \alpha^2 + \beta^2$, $\frac{d}{dy}$ and $\frac{d^2}{dy^2}$ are, respectively, the first and second differentiation matrices along the wall-normal coordinate, and Z is the zeros matrix. No-slip conditions at the walls are applied to the linear operator.

The input matrix B is given by

$$B = \begin{bmatrix} I & Z & Z \\ Z & I & Z \\ Z & Z & I \\ Z & Z & Z \end{bmatrix}, \tag{8}$$

with the rows corresponding to the wall positions for the three-momentum equations set to zero to enforce the boundary conditions.

To restrict the observations to the pressure field, operator C is defined in this work as

$$C = [Z \quad Z \quad Z \quad I]. \tag{9}$$

The linear operator can include an eddy-viscosity model. Following Towne *et al.* [46], the linear operator L including the Cess eddy-viscosity model [38] reads

$$L = \begin{bmatrix} i\alpha\bar{U} - i\omega I - E - J & -i\alpha\nu_T'I + \frac{d\bar{U}}{dy} & Z & i\alpha I \\ Z & i\alpha\bar{U} - i\omega I - 2E - J & Z & \frac{d}{dy} \\ Z & -i\beta\nu_T'I & i\alpha\bar{U} - i\omega I - E - J & i\beta I \\ i\alpha I & \frac{d}{dy} & i\beta I & Z \end{bmatrix}, \tag{10}$$

where $\nu_T{}' = \frac{d}{dy}\nu_T$, $\boldsymbol{E} = \nu_T{}'\frac{d}{dy}$, and $\boldsymbol{J} = \frac{1}{\mathrm{Re}_\tau}\frac{\nu_T}{\nu}\nabla^2$. The total eddy viscosity $\nu_T(y)$, obtained after the sum of the turbulent eddy viscosity $\nu_t(y)$ and the viscosity ν, is modeled as

$$\frac{\nu_T}{\nu} = \frac{1}{2}\left\{1 + \frac{\kappa^2\mathrm{Re}_\tau{}^2}{9}[1-(\eta-1)^2]^2[1+2(\eta-1)^2]^2\left[1-e^{(|\eta-1|-1)\mathrm{Re}_\tau/A}\right]^2\right\}^{1/2} + \frac{1}{2}, \quad (11)$$

where the constants κ and A are constants given as 0.426 and 25.4, respectively [40], and η is the nondimensional wall distance in outer units, i.e., $\eta = y/H$ and $y \in [0, 2H]$ (i.e., $\eta \in [0, 2]$).

The application of SVD on the resolvent operator accounting for the integration weights leads to

$$\boldsymbol{K}_p{}^{1/2}\boldsymbol{H}\boldsymbol{K}_f{}^{-1/2} = \tilde{\boldsymbol{U}}\boldsymbol{\Sigma}\tilde{\boldsymbol{V}}^\dagger, \quad (12a)$$

$$\boldsymbol{V} = \boldsymbol{K}_f{}^{-1/2}\tilde{\boldsymbol{V}}, \quad (12b)$$

$$\boldsymbol{U} = \boldsymbol{R}\boldsymbol{B}\boldsymbol{V}, \quad (12c)$$

where the columns of $\boldsymbol{U}$ and $\boldsymbol{V}$ form orthonormal bases, $\boldsymbol{\Sigma}$ is a rectangular diagonal matrix of singular values, and $\dagger$ denotes the Hermitian operator. $\boldsymbol{U} = [\boldsymbol{U}_1\,\boldsymbol{U}_2\,\dots\,\boldsymbol{U}_n]$ and $\boldsymbol{V} = [\boldsymbol{V}_1\,\boldsymbol{V}_2\,\dots\,\boldsymbol{V}_n]$ can be interpreted as the optimal output (response or resolvent) and input (forcing) modes, respectively. The gain matrix $\boldsymbol{\Sigma}$ is diagonal with real, positive and decreasing values, i.e., $\sigma_1 \geqslant \sigma_2 \geqslant \cdots \geqslant \sigma_n$. A harmonic forcing $\hat{\boldsymbol{f}} = \boldsymbol{V}_i$ leads to a flow response $\hat{\boldsymbol{q}} = \sigma_i\boldsymbol{U}_i$. For $n = 1$, the pair $(\boldsymbol{U}_1, \boldsymbol{V}_1)$ provides the optimal, or most amplified, forcing and its associated response [23,24]. When $\sigma_1 \gg \sigma_2$, i.e., there exists a large gain separation between the first two singular values, the first response mode tends to dominate the flow and the operator is denominated as low-rank.

Tilde notations in Eq. (12c) indicate quantities biased by the integration weights, with the Cholesky decomposition denoted by $\boldsymbol{K}_p{}^{1/2}$ and $\boldsymbol{K}_f{}^{1/2}$ regarding the pressure and forcing components, respectively. $\boldsymbol{K}_p$ is a diagonal matrix containing Clenshaw-Curtis quadrature weights [47] and $\boldsymbol{K}_f$ is defined as

$$\boldsymbol{K}_f = \begin{bmatrix} \boldsymbol{K}_p & \boldsymbol{Z} & \boldsymbol{Z} \\ \boldsymbol{Z} & \boldsymbol{K}_p & \boldsymbol{Z} \\ \boldsymbol{Z} & \boldsymbol{Z} & \boldsymbol{K}_p \end{bmatrix}. \quad (13)$$

Note that if one defines Eq. (12c) as

$$\boldsymbol{U} = \boldsymbol{C}\boldsymbol{R}\boldsymbol{B}\boldsymbol{V} = \boldsymbol{H}\boldsymbol{V} = \boldsymbol{K}_p{}^{-1/2}\tilde{\boldsymbol{U}}, \quad (14)$$

then the resolvent modes would be restricted by the pressure fluctuation component, i.e., only pressure modes could be recovered. Defining Eq. (12c) as $\boldsymbol{U} = \boldsymbol{R}\boldsymbol{B}\boldsymbol{V}$ enables the recovering of the full-state modes, i.e., velocity and pressure fluctuation components.

C. Two-point statistics (CSD)

Let us consider

$$\boldsymbol{Q} = \langle\hat{\boldsymbol{q}}\hat{\boldsymbol{q}}^\dagger\rangle, \quad (15a)$$

$$\boldsymbol{F} = \langle\hat{\boldsymbol{f}}\hat{\boldsymbol{f}}^\dagger\rangle, \quad (15b)$$

where $\boldsymbol{Q}$ and $\boldsymbol{F}$ are the CSDs, or the two-point statistics, of the state and forcing components as a function of (α, β, ω) and symbol $\langle\dots\rangle$ denoting the expected-value operator. Welch's method [48] can be employed to evaluate a CSD from a time series.

It is possible to obtain the flow response to an stochastic process employing the resolvent operator [26,28,29], i.e.,

$$\boldsymbol{S} = \boldsymbol{H}\boldsymbol{F}\boldsymbol{H}^\dagger. \quad (16)$$

Moreover, the observation CSD can be obtained as

$$Y = CQC^\dagger. \tag{17}$$

Expression (16) is the input-output relation between the forcing (F) and response (S) CSDs. Knowledge of the full forcing statistics terms allows the recovery of the full response statistics. If the forcing statistics terms are unknown, then one option is to model it as white noise, i.e., $F = I$ and hence

$$S_I = HH^\dagger. \tag{18}$$

In practical applications, typically the forcing CSD terms are unknown and modeling them as white noise is an interesting possibility. Yet, one may include an eddy-viscosity model in the linear operator formulation to account for part of the forcing terms maintaining the forcing CSD as white noise, i.e.,

$$S_{\nu_T} = H_{\nu_T} H_{\nu_T}^\dagger, \tag{19}$$

where subscript ν_T indicates the use of the eddy-viscosity model within the resolvent operator.

D. SPOD

SPOD is a technique that decomposes a set of snapshots into an orthonormal, optimal basis in the frequency domain [26,49,50]. The obtained modes represent structures that maximize the mean-square energy of the analyzed flow field for a given inner product [51].

The SPOD can be evaluated by taking the eigenvalue decomposition of the CSD of the state (or forcing) for a triplet (α, β, ω) and an appropriate weight or inner product. In discrete form, the generalized problem can be written as

$$DW\Psi = \Psi\Lambda, \tag{20}$$

where D is the CSD of interest, e.g., state observations [Y, Eq. (17)] or forcing [F, Eq. (15b)], W accounts for both the integration weights and the numerical quadrature on the discrete grid, Ψ denotes the SPOD modes, and Λ corresponds to the eigenvalues.

The SPOD modes are an orthonormal basis that optimally represent the CSD of interest, in the present case the pressure fluctuations, for a given wave number–frequency combination [26]. The contribution of each SPOD mode (eigenfunction) to the CSD representation is given by its associated eigenvalue, ranked according to the energetic content, i.e., from the most to the least energetic, i.e., $\lambda_1 \geqslant \lambda_2 \geqslant \cdots \lambda_n$.

To extract the SPOD modes, we followed the procedures by Towne *et al.* [26] and Schmidt and Towne [27]. Therefore, we have not solved Eq. (20) but an equivalent problem that contains the same nonzero eigenvalues, given by

$$\hat{G}^\dagger W \hat{G} \Theta = \Theta \tilde{\Lambda}, \tag{21a}$$

$$\tilde{\Psi} = \hat{G} \Theta \tilde{\Lambda}^{-1/2}, \tag{21b}$$

where $\hat{G}$ is a matrix containing the state (or forcing) Fourier transforms of each data block, Θ denotes the eigenvectors, $\tilde{\Lambda}$ stands for the eigenvalues, and $\tilde{\Psi}$ contains the SPOD modes. The total number of nonzero eigenvalues is N_b, i.e., the same as the number of blocks employed in the Welch's method to obtain the CSDs.

To target the pressure SPOD, operator W is defined as

$$W = \begin{bmatrix} Z & Z & Z & Z \\ Z & Z & Z & Z \\ Z & Z & Z & Z \\ Z & Z & Z & K_p \end{bmatrix}, \tag{22}$$
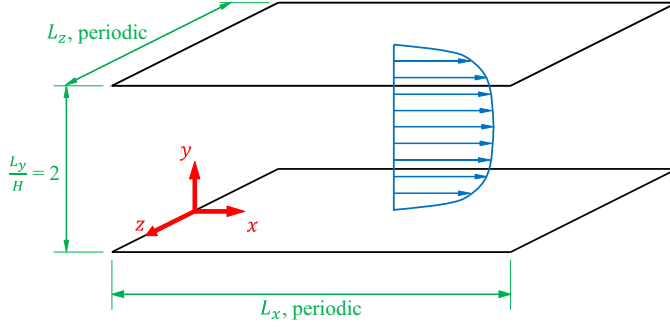
FIG. 1. Sketch of the channel flow geometry (black), coordinate system (red), and mean flow (blue) together with relevant dimensions (green).

whereas $\hat{G}$ is a matrix that is organized, for each frequency ω and wave-number pair (α, β), as containing the Fourier transforms of each state component and for each wall-normal distance y in its lines, i.e., N_y lines (N_y being the mesh discretization in the wall-normal direction), and the columns are organized in terms of data blocks, i.e., N_b columns. Therefore,

$$\hat{G} = \begin{bmatrix} \hat{q}_1 & \hat{q}_2 & \cdots & \hat{q}_{N_b} \end{bmatrix}, \tag{23}$$

for a triplet (α, β, ω) and

$$\hat{q} = \kappa [\hat{u}_x \quad \hat{u}_y \quad \hat{u}_z \quad \hat{p}]^T, \tag{24}$$

where the state components are written in the frequency–wave number domain, i.e., for a triplet (α, β, ω), and κ is a constant defined as

$$\kappa = \frac{1}{\sqrt{N_b \Delta f}}, \tag{25}$$

where Δf is the frequency discretization.

It is important to remark that resolvent and SPOD modes are identical when the forcing CSD is considered white in space, with the SPOD eigenvalues equal to the square of the resolvent modes [26].

E. Numerical simulations

The ChannelFlow pseudospectral code [52] was employed to conduct the DNS of incompressible turbulent channel flow for friction Reynolds numbers of $\mathrm{Re}_\tau \approx 180$ and 550. In Cartesian coordinates, with half height H used for normalization, the boxes dimensions are $4\pi \times 2 \times 2\pi$ in the streamwise (L_x), wall-normal (L_y), and spanwise (L_z) directions, respectively, for the $\mathrm{Re}_\tau \approx 180$ simulation, and $2\pi \times 2 \times \pi$ for the $\mathrm{Re}_\tau \approx 550$ case. The wall-normal direction is defined within $y/H \in [0, 2]$. Figure 1 shows a sketch of the flow geometry employed in the simulations.

For each simulation, the state and forcing components were stored as a function of time t, wall-normal distance y, and streamwise and spanwise wave numbers, α and β, respectively, i.e., $q = q(\alpha, y, \beta, t)$ and $f = f(\alpha, y, \beta, t)$. Chebyshev polynomials were employed for the discretization of the wall-normal direction (y), whereas the streamwise (x) and spanwise (z) directions were discretized using Fourier modes; the collocation points in the streamwise and spanwise directions were expanded by a $3/2$ factor for dealiasing purposes [10].

Table I shows the simulation main parameters, including the bulk Reynolds numbers Re and the friction Reynolds numbers Re_τ, the number of mesh points (N_x, N_y, and N_z) and mesh discretization (Δx^+, Δz^+, $\Delta y_{\min}^+$, and $\Delta y_{\max}^+$). The first column of the table contains the canonical values for the friction Reynolds number and, between parenthesis, their actual value from the simulations.

TABLE I. DNS parameters of the two channel flow cases addressed in the present study.

Re_τ	Re	N_x	N_y	N_z	Δx^+	Δz^+	$\Delta y_{min}{}^+$	$\Delta y_{max}{}^+$	N_t	Δt^+	N_{fft}	N_b
180 (179)	2800	192	129	192	11.71	5.86	5.39×10^{-2}	4.39	2399	5.72	64	146
550 (543)	10 000	384	257	384	8.89	4.44	4.09×10^{-2}	6.66	3000	2.95	64	184

The plus superscript indicates nondimensional quantities using inner (viscous) scaling. Table I also includes information on the number of snapshots (N_t) and the time steps based on inner units (Δt^+), as well as the block-size (N_{fft}) and number-of-blocks (N_b) employed to evaluate CSDs and PSDs. The computation of power spectra, CSDs and PSDs of the flow state and forcing were performed using Welch's method [48] with a Hann window and blocks containing 75% overlap.

The works by Martini *et al.* [53] and Morra *et al.* [44] present the DNS validation results for the mean velocity profile and root-mean-square (rms) values of velocity components; the former paper for $Re_\tau \approx 180$ and the later for $Re_\tau \approx 550$. Literature results from earlier simulations [54] were employed for validation purposes. Pressure statistics validation results were not addressed by Martini *et al.* [53] and Morra *et al.* [44]. Therefore, Fig. 2 displays the root-mean-square of the pressure component for the present database (continuous lines) and for the data obtained from del Álamo and Jiménez [54] (symbols), which show good agreement.

To further validate the DNS databases, Fig. 3 displays one-sided wall-pressure spectra scaled in inner units as a function of streamwise (left frame) and spanwise (right frame) wave numbers. Comparisons among the results of the present simulations with others obtained in the literature [11,13] are displayed in the figure. Note the $Re_\tau \approx 550$ database has a higher friction Reynolds number than the one used by Anantharamu and Mahesh [13], which is 400. Regarding the streamwise wave-number spectra (left frame), good agreement is achieved for the energy containing part of the spectrum at low wave numbers. Differences with respect to the $Re_\tau = 400$ case in Anantharamu and Mahesh [13] may be attributed to the different Reynolds numbers of the simulations. The high-wave-number content of the present simulation has a faster decay than earlier results. This may be related to the use of the rotational form of the nonlinear terms in the present simulation, as different choices for the nonlinear terms may affect results [55]. As the present study focuses on larger pressure structures, the agreement at lower wave numbers and rms profiles was considered sufficient.

(a) $Re_\tau \approx 180$
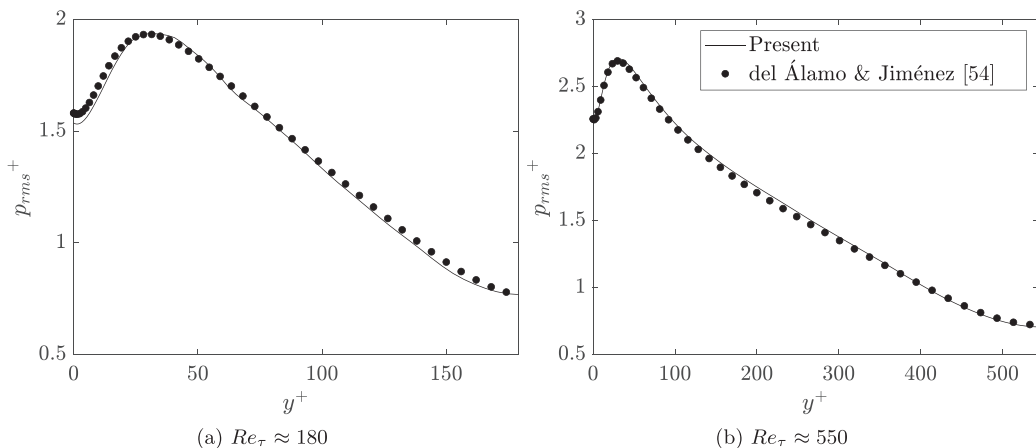
(b) $Re_\tau \approx 550$

FIG. 2. Comparison between the pressure component rms for the present simulations (continuous lines) and those by del Álamo and Jiménez [54] (symbols).
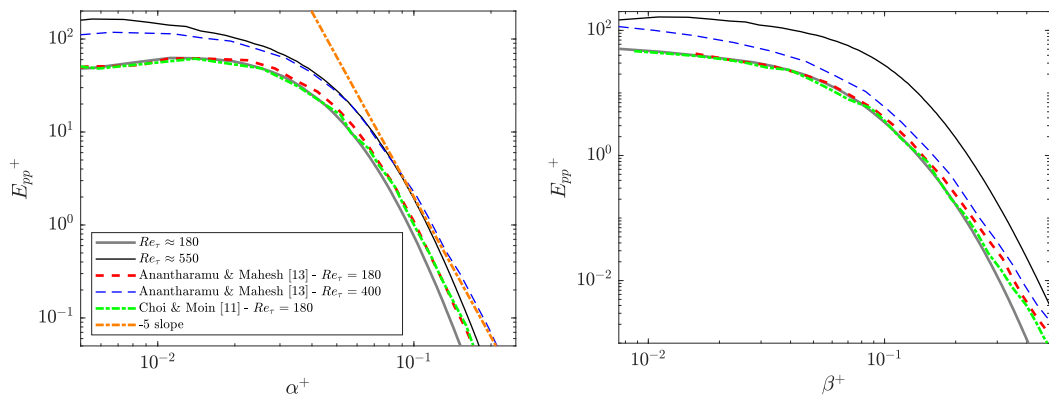
FIG. 3. Comparison among wall-pressure fluctuation streamwise wave-number spectra for the present $Re_\tau \approx 180$ (gray thick continuous line) and 550 (black thin continuous line) simulations and the results by Anantharamu and Mahesh [13] at $Re_\tau \approx 180$ (red thick dashed line) and 400 (blue thin dashed line) and by Choi and Moin [11] at $Re_\tau \approx 180$ (green thick dash-dotted line). Left frame: Spectra as a function of streamwise wave number in inner units. Right frame: Spectra as a function of spanwise wave number in inner units. A -5 slope curve (orange thick dotted line) is also plotted in the left frame.

The present turbulent channel flow simulations have statistical symmetry around the central plane. We take advantage of this by decomposing fluctuations into even and odd parts around the central plane, as in Abreu *et al.* [32]. In this study we considered the odd part of pressure fluctuations, with the corresponding even or odd parts for the other state and forcing components.

III. WAVE-NUMBER AND FREQUENCY SPECTRA OF PRESSURE FLUCTUATIONS

We start by evaluating wave-number and frequency spectra for the pressure in order to select the most energetic structures for further analysis. The procedure will follow the approach of Morra *et al.* [56], this time for pressure fluctuations. Spectra without and with premultiplication will be used, since, as will be shown, energetic spanwise-coherent pressure structures appear in the spectrum without premultiplication. A detailed analysis of the $Re_\tau \approx 550$ channel flow will be addressed in the following, whereas complementary results for the $Re_\tau \approx 180$ simulation are displayed in Appendix.

The pressure component spectra at the channel wall ($y = 0$) and at $y^+ \approx 100, 200$ and $y \approx 0.5$ (a height characteristic of large-scale structures [54]) are shown in Figs. 4 and 5 for the pressure power spectra with and without premultiplication, respectively. Minor differences between wall ($y = 0$) and buffer-layer spectra ($y^+ \approx 15$, characteristic of near-wall structures) were observed and hence we decided to show only the results on the channel wall. The wall premultiplied spectrum peaks at $(\lambda_x^+, \lambda_z^+) \approx (227, 155)$ and the λ_x^+ peak value agrees with previous studies [13,16]. On the other hand, the $y \approx 0.5$ plane premultiplied spectrum peaks at $(\lambda_x, \lambda_z) \approx (0.90, 1.57)$. The premultiplied spectra at $y^+ \approx 100$ resembles the one at $y = 0$, although the energy peak moved to slightly higher wavelengths, whereas the spectra at $y^+ \approx 200$ resembles the one at $y \approx 0.5$ (equivalent to $y^+ \approx 270$). Note that on the wall ($y = 0$), peak spectral wave numbers denote structures that are streamwise elongated, i.e., $\lambda_x > \lambda_z$, whereas far from the wall (e.g., $y \approx 0.5$), the more energetic structures are spanwise elongated, i.e., $\lambda_z > \lambda_x$.

The pressure spectra without premultiplication as a function of streamwise and spanwise wave numbers shown in Fig. 5 peaks at $(\alpha, \beta) = (3, 0)$ for all the four studied planes, suggesting the presence of large spanwise elongated structures extending throughout the channel. This peak wave number matches the results of Yang and Yang [14]. Abreu *et al.* [57] and Pozuelo *et al.* [58] verified that such spanwise elongated structures ($\beta = 0$) for velocity fluctuations are not an artifact of small
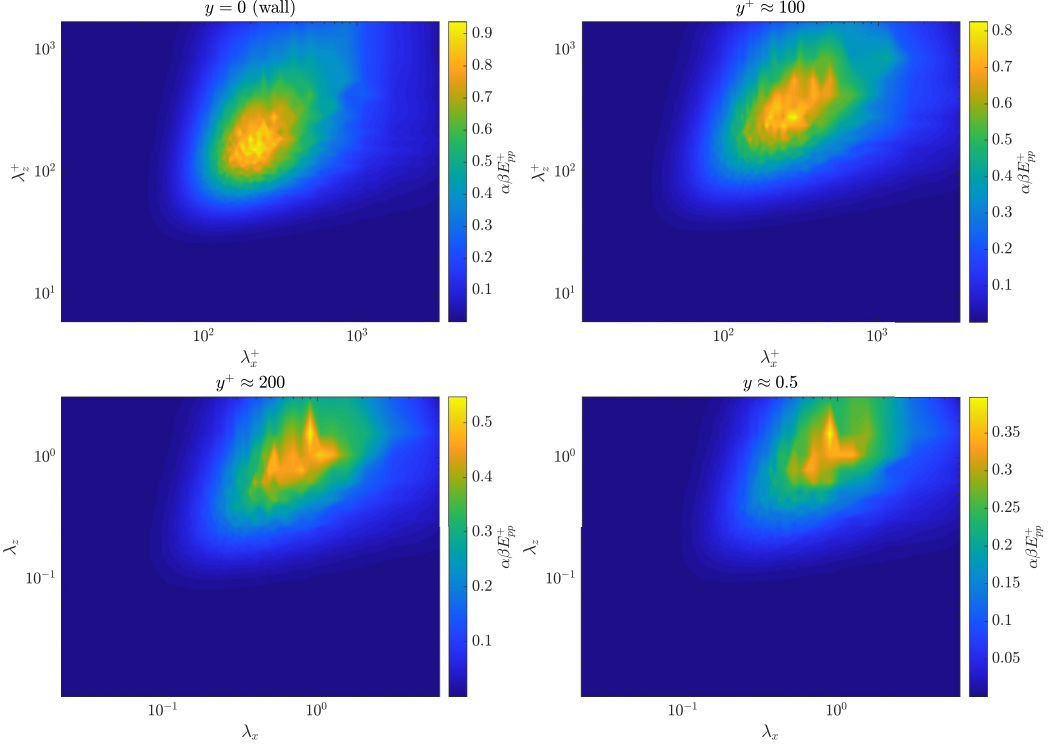
FIG. 4. Premultiplied energy spectra for $\mathrm{Re}_\tau \approx 550$ simulation.

domains. Spanwise-elongated pressure structures are potentially relevant for problems involving fluid-structure interaction [59] and sound radiation [60,61]. Hereinafter, as a convention, we will refer to the near-wall structures in inner (or wall) units, whereas large-scale structures will be dealt with using outer units. We will also focus on the near-wall ($y = 0$), large-scale ($y \approx 0.5$) and the spanwise-coherent structures.

To determine frequencies of interest for the peak wave numbers, similarly to what was done by Morra *et al.* [56], the pressure PSD for near-wall and large-scale structures are exhibited in the top frames of Fig. 6 as a function of wall-normal distance and phase speed. In the figure, the PSD is plotted as a function of the wall-normal distance and phase speed $c^+ = \omega^+/\alpha^+$, where ω^+ is the angular frequency scaled in inner units. The top and bottom frames correspond to the PSD of the pressure and streamwise forcing components, respectively. The figure also shows the critical layer ($U^+ = c^+$) in dashed lines. The pressure component PSDs peak at $c^+ \approx 13.5$ ($\omega^+ \approx 0.37$) with support at $y^+ \approx 30$ and $c^+ \approx 18$ ($\omega \approx 6.87$) with support at $y \approx 0.38$ for the near-wall and large-scale structures, respectively. The ω^+ peak value is in agreement with previous results [12,13]. For the forcing streamwise component, the PSDs peak at $c^+ \approx 12$ and 13 for the near-wall and large-scale structures, respectively, both with support at $y^+ \approx 10$. Such near-wall nature of the forcing peak, even for large-scale structures, was reported by Morra *et al.* [44].

The PSDs are shown in Fig. 7 for the pressure (right frame) and streamwise forcing (left frame) components for the spanwise-coherent structures with $(\alpha, \beta) = (3, 0)$. Both pressure and forcing components PSD peak at $\omega \approx 2.95$, the first with support at $y^+ \approx 183$, following the critical layer, and the latter with support at $y^+ \approx 7$. Hereinafter, the power spectra without premultiplication peak will be refereed to as PSP.

Table II summarizes the results of the preceding analysis of spectra for both Reynolds numbers. The spectral peaks are given in terms of spanwise and streamwise wave numbers and wavelengths
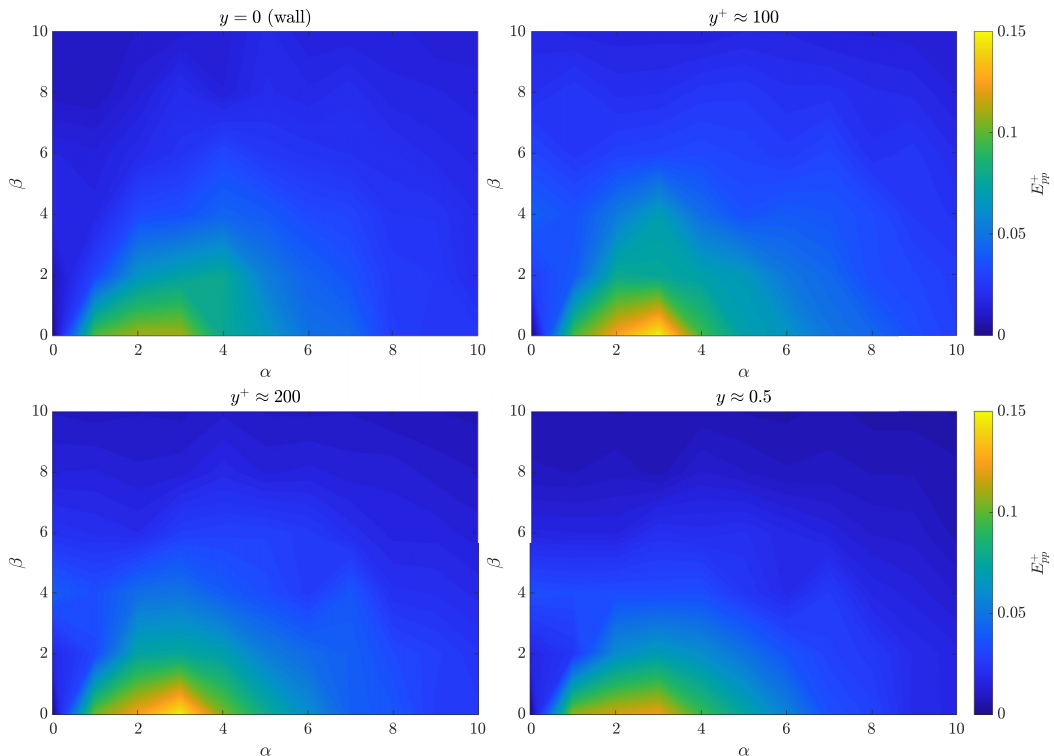
FIG. 5. Energy spectra for $\mathrm{Re}_\tau \approx 550$ simulation.

(in inner and outer units), phase speeds, angular frequencies (in inner and outer units) and wall-normal distance of the peak (in inner and outer units) for both Reynolds numbers. Results for the pressure and streamwise forcing spectra are shown in the table, and when the peak location of the latter is different from the former ones, such values are provided between parenthesis. Note that it is also possible to recover the temporal wavelengths through the relationships $\lambda_t = 2\pi/\omega$ and $\lambda_t^+ = 2\pi/\omega^+$ in outer and inner units, respectively. The near-wall structures for both Reynolds numbers show similar peak location when considering inner scaling, i.e., $(\lambda_x^+, \lambda_z^+) \approx (200, 160)$ and $(c^+, \omega^+) \approx (13.5, 0.4)$, with support at $y^+ \approx 35$, whereas for the streamwise forcing component, one has $(c^+, \omega^+) \approx (12, 0.35)$. Such scaling must be taken with care, since only two moderate Reynolds numbers are considered in the present study. For completeness, results for the wall-normal distance of $y^+ \approx 15$ are also provided in the table and it is verified that the spectral characteristics at this distance are very similar to those obtained at the wall ($y = 0$). For the large-scale structures ($y \approx 0.5$), no obvious scaling with either inner or outer units is observed. Regarding the spectra without premultiplication, large structures that are infinitely long in the spanwise direction were found for both Reynolds numbers. Analyzing the forcing spectra, such spanwise-coherent structures have at $y^+ \approx 7$ for both Reynolds numbers, whereas the pressure spectra show support at $y^+ \approx 44$ and 183 for $\mathrm{Re}_\tau \approx 180$ and 550, respectively.

IV. COMPARISON BETWEEN SPOD AND RESOLVENT MODES

A. Dominant structures

The dominant coherent structures described in the previous section are further explored using SPOD and resolvent analysis for the $\mathrm{Re}_\tau \approx 550$ simulation. Appendix displays complementary
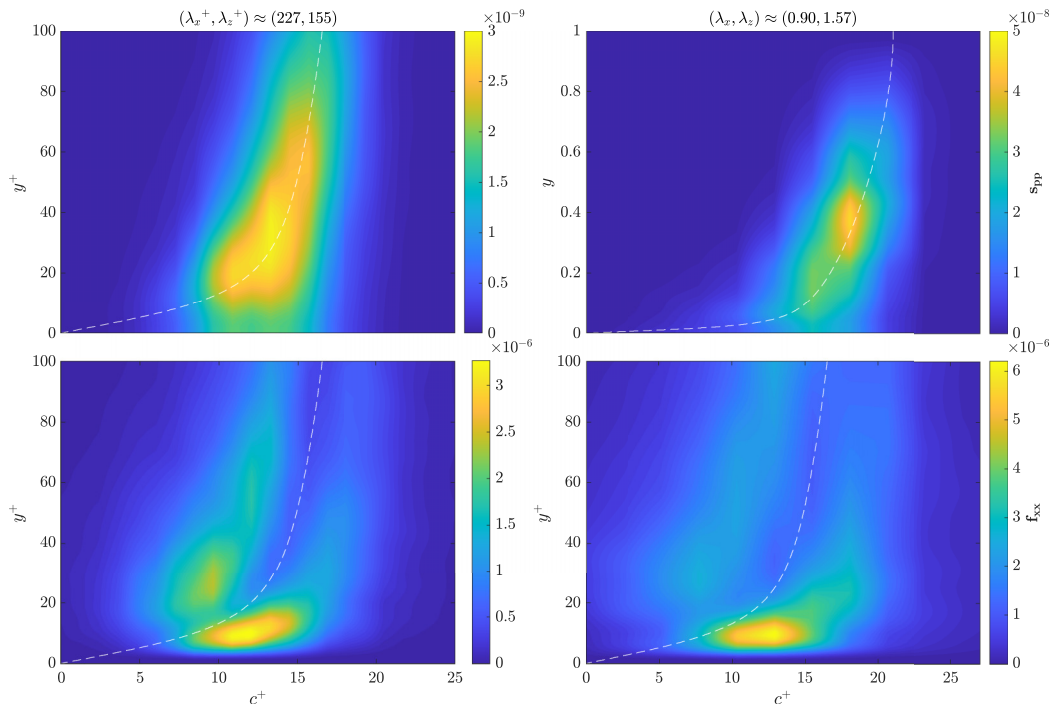
FIG. 6. PSDs for $\mathrm{Re}_\tau \approx 550$ simulation. Left frames: Near-wall structures. Right frames: Large-scale structures. Top frames: Pressure component (s_{pp}). Bottom frames: Streamwise forcing component ($\boldsymbol{f}_{xx}$). Dashed lines denote the critical layer. Note the vertical axis scaling of the top-left frame is in outer units (y), whereas the other frames retained inner units (y^+).

results for the $\mathrm{Re}_\tau \approx 180$ simulation. Regarding the resolvent analysis, results without and with the eddy-viscosity model are addressed.

Figure 8 exhibit the SPOD eigenvalues evaluated for the pressure (top frames) and forcing (bottom frames) components. Near-wall, large-scale, and spanwise-coherent structures are displayed in the left, middle, and right frames, respectively. The first SPOD eigenvalue correspond to
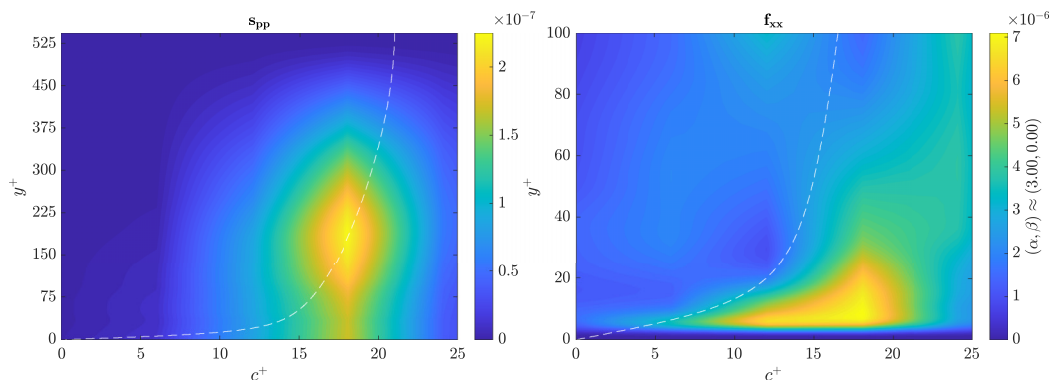
FIG. 7. PSDs for $\mathrm{Re}_\tau \approx 550$ simulation and spanwise-coherent structure, i.e., $(\alpha, \beta) = (3, 0)$. Right frame: Pressure component (s_{pp}). Left frame: Streamwise forcing component ($\boldsymbol{f}_{xx}$). Dashed lines denote the critical layer.

TABLE II. Spectral peaks for wall, near-wall, large-scale, and PSP structures for the two Reynolds numbers studied. Notation *w/pm* indicates spectra with premultiplication, whereas *w/o pm* pm indicates spectra without premultiplication. When the streamwise forcing component peak location differs from those of the pressure component, the values of the forcing peak are given between parenthesis. y_{peak}^+ and y_{peak} denote the PSD peak position.

	λ_x^+	λ_z^+	λ_x	λ_z	α	β	c^+	ω^+	ω	y_{peak}^+	y_{peak}
w/pm, $y = 0$, $\text{Re}_\tau \approx 180$	204	161	1.14	0.90	5.5	7	14 (12.5)	0.43 (0.38)	4.91 (4.32)	38 (10)	0.21 (0.06)
w/pm, $y^+ \approx 15$, $\text{Re}_\tau \approx 180$	225	125	1.26	0.70	5	9	14 (12.5)	0.40 (0.34)	4.52 (3.93)	33 (10)	0.17 (0.06)
w/pm, $y \approx 0.5$, $\text{Re}_\tau \approx 180$	250	375	1.40	2.09	4.5	3	16 (12.5)	0.39 (0.31)	4.52 (3.53)	76 (10)	0.42 (0.06)
w/o pm, $\text{Re}_\tau \approx 180$	749	∞	12.57	∞	0.5	0	12.5	0.03	0.39	44 (6.5)	0.24 (0.04)
w/pm, $y = 0$, $\text{Re}_\tau \approx 550$	227	155	0.42	0.29	15	22	13.5 (12)	0.37 (0.33)	10.8(9.82)	30 (10)	0.05 (0.02)
w/pm, $y^+ \approx 15$, $\text{Re}_\tau \approx 550$	227	131	0.42	0.24	15	26	12 (13)	0.33 (0.37)	9.82 (10.80)	20 (10)	0.04 (0.02)
w/pm, $y \approx 0.5$, $\text{Re}_\tau \approx 550$	490	850	0.90	1.57	7	4	18 (13)	0.23 (0.17)	6.87 (4.91)	209 (10)	0.38 (0.02)
w/o pm, $\text{Re}_\tau \approx 550$	1137	∞	2.09	∞	3	0	18	0.10	2.95	183 (7)	0.34 (0.01)

approximately 61%, 69%, and 91% of the total energy for the near-wall, large scale, and spanwise-coherent structures, respectively, when considering the pressure component. Abreu *et al.* [32] report a first eigenvalue corresponding to about 68% and 84% of the total energy for the near-wall and large-scale structures, respectively. Note that the near-wall and large-scale structures obtained by Abreu *et al.* [32] peak at other spatial and temporal wavelengths, since they are targeting the streamwise velocity component and consider the kinetic energy weighting to evaluate the SPOD modes. If the forcing components are considered instead, then the first SPOD eigenvalues decay to approximately 25%, 21%, and 27% of the total energy for the respective structures. Taking into account the second forcing SPOD eigenvalue raises the percentile contribution to approximately 43%, 37%, and 41%, respectively. However, the leading pressure SPOD mode remains strongly dominant for the three considered structures.

Figure 9 displays the resolvent and eddy-viscosity resolvent gains, where black circle markers indicate the former and red square markers account for the latter. Frames, from left to right, denote the near-wall, large-scale and spanwise-coherent structures, respectively. The ratio between the first and second resolvent gains, i.e., σ_1/σ_2, is of approximately 3.94, 9.52, and 30.85 for the
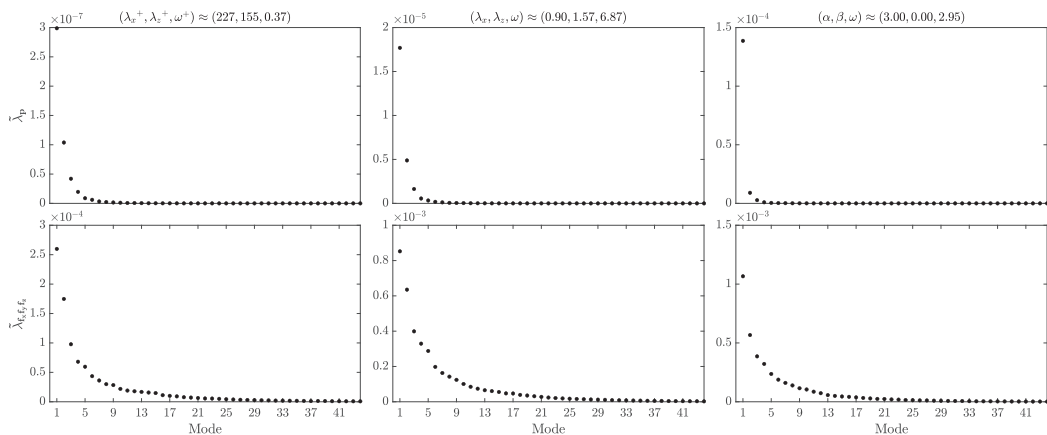

FIG. 8. SPOD eigenvalues employing the pressure (top frames) and forcing (bottom frames) modes for the $\text{Re}_\tau \approx 550$ simulation. Frames from left to right: Near-wall, large-scale, and spanwise-coherent structures, respectively.
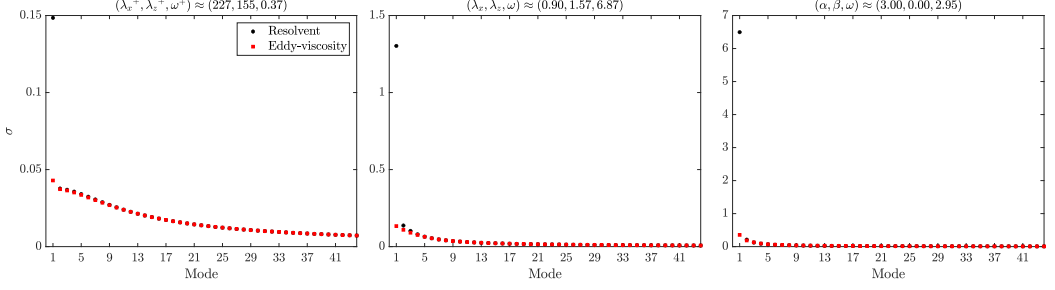
FIG. 9. Resolvent gains employing the pressure weighing for the $Re_\tau \approx 550$ simulation. Black circles: Linear operator without eddy-viscosity model. Red squares: Linear operator with eddy-viscosity model. See the comments in the caption of Fig. 8.

near-wall, large scale and spanwise-coherent structures, respectively, i.e., a low-rank behavior is observed. Regarding the eddy-viscosity resolvent gains, such low-rank behavior is not present, with suboptimal gains close to the optimal ones.

Low-rank reconstructions of the pressure PSD [$\boldsymbol{P}_{pp}^{(est)}$] for the near-wall and large-scale structures are displayed in Fig. 10 using only the first resolvent or response mode, i.e.,

$$\boldsymbol{P}_{pp}^{(est)} = a_{corr} \boldsymbol{U}_1 {\sigma_1}^2 {\boldsymbol{U}_1}^\dagger, \tag{26}$$

where a_{corr} is the amplitude correction factor, chose to match the DNS [$\boldsymbol{P}_{pp}^{(DNS)}$, Figs. 6 and 7] at each frequency ω as

$$a_{corr}(\omega) = \frac{\int_{y/H=0}^{2} \boldsymbol{P}_{pp}^{(DNS)}(\alpha, y, y, \beta, \omega) dy}{\int_{y/H=0}^{2} \boldsymbol{U}_1 {\sigma_1}^2 {\boldsymbol{U}_1}^\dagger dy}, \tag{27}$$

in the same fashion as Morra *et al.* [56].

In comparison with the top frames of Fig. 6, it is seen that the near-wall and large-scale structures are well represented by the first mode. This feature is somewhat expected since a gain separation of approximately one order of magnitude is observed for such structure (Fig. 9). However, the predictions from resolvent analysis without eddy-viscosity tend to be more concentrated around the critical layer $c = U$ than the trends from DNS data [56]; this feature is observed in the plots. Regarding the spanwise-coherent structure, an even closer match with the DNS PSD is obtained, peaking at $(c^+, y^+) \approx (18, 180)$; again, the gain separation is significant, which leads to a clearly dominant mechanism for spanwise-coherent structures.
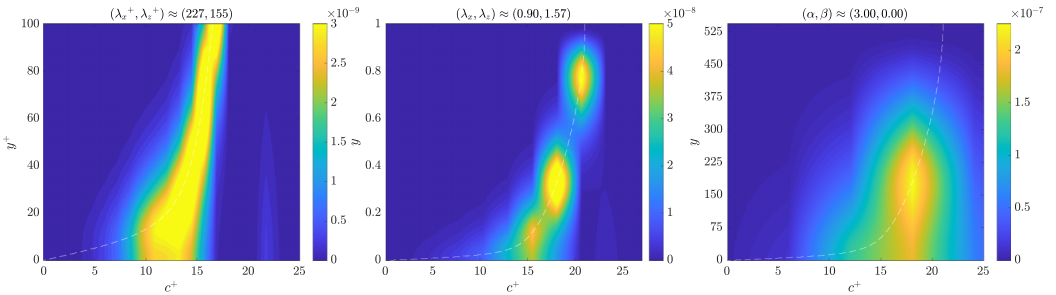

FIG. 10. Pressure component PSD low-rank resolvent reconstruction (first mode) for the $Re_\tau \approx 550$ simulation. Frames from left to right: near-wall, large-scale, and spanwise-coherent structures, respectively.
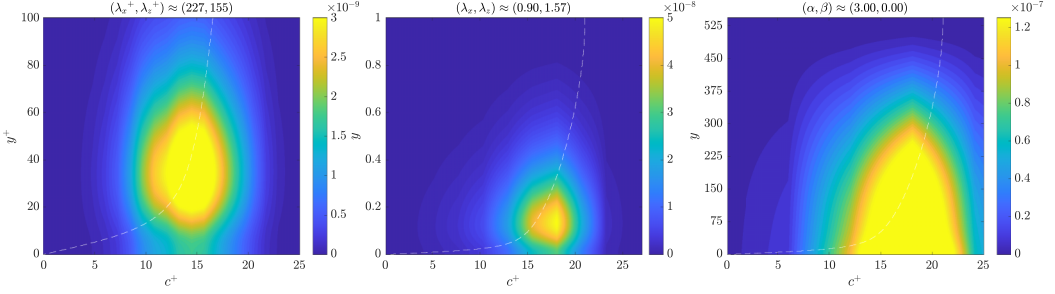
FIG. 11. Pressure component PSD low-rank eddy-viscosity resolvent reconstruction (first mode) for the $Re_\tau \approx 550$ simulation. See the comments in the caption of Fig. 10.

Figure 11 shows the low-rank reconstructions now using the eddy-viscosity resolvent, i.e.,

$$\boldsymbol{P}_{pp}^{\nu_T\,(\text{est})} = a_{\text{corr}}^{\nu_T}\boldsymbol{U}_1^{\nu_T}\sigma_1^{\nu_T\,2}\boldsymbol{U}_1^{\nu_T\,\dagger}, \tag{28}$$

with

$$a_{\text{corr}}^{\nu_T}(\omega) = \frac{\int_{y/H=0}^{2}\boldsymbol{P}_{pp}^{(\text{DNS})}(\alpha, y, y, \beta, \omega)dy}{\int_{y/H=0}^{2}\boldsymbol{U}_1^{\nu_T}\sigma_1^{\nu_T\,2}\boldsymbol{U}_1^{\nu_T\,\dagger}dy}. \tag{29}$$

Although this model does not show a low-rank behavior (Fig. 9), it captured the energy peak position for the near-wall structures at $(c^+, y^+) \approx (13.5, 30)$. In contrast, the eddy-viscosity resolvent does not well represent the energy peak position for the large-scale structure, which shows a peak at $(c^+, y) \approx (16, 0.1)$, and for the spanwise-coherent structure, which only the phase speed peak is correct at $c^+ \approx 18$. Besides the mismatch in pressure PSD peaks, the distributions along y are not well represented by the low-rank reconstruction.

SPOD ($\tilde{\boldsymbol{\Psi}}_p$), resolvent ($\boldsymbol{U}$), and eddy-viscosity resolvent ($\boldsymbol{U}^{\nu_T}$) modes are shown in Fig. 12 for the near-wall and large-scale structures. For brevity, only the first SPOD and the optimal resolvent and eddy-viscosity resolvent modes are shown. The pressure component is depicted in the contours, where blue color denotes negative values, whereas the red color indicates positive values in the
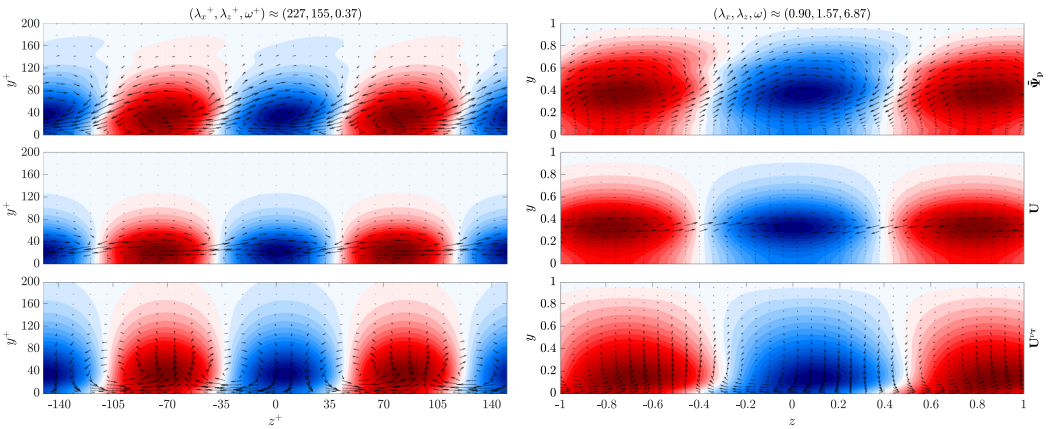

FIG. 12. Pressure near-wall (left frames) and large-scale (right frames) structures modes for the $Re_\tau \approx 550$ simulation. Rows (from top to bottom): First SPOD ($\tilde{\boldsymbol{\Psi}}_p$), resolvent ($\boldsymbol{U}$), and eddy-viscosity resolvent ($\boldsymbol{U}^{\nu_T}$) modes. Contours correspond to the pressure component, with blue associated to negative pressure and red associated to positive pressure. Arrows denote wall-normal and spanwise velocity components.
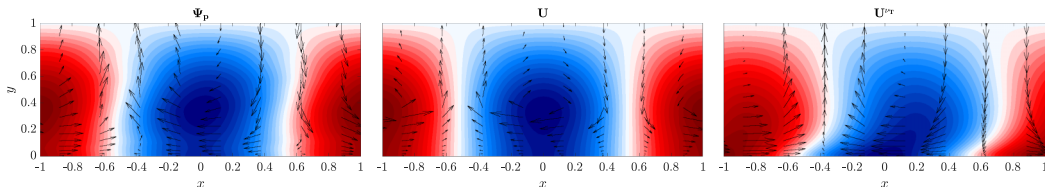
FIG. 13. Pressure spanwise-coherent structures for the $Re_\tau \approx 550$ simulation. Frames (from left to right): First SPOD ($\tilde{\mathbf{\Psi}}_p$), resolvent ($\mathbf{U}$), and eddy-viscosity resolvent ($\mathbf{U}^{\nu_T}$) modes. See the comments in the caption of Fig. 12.

color map scale. For all frames, the arrows correspond to the wall-normal and spanwise velocity components; although SPOD targets pressure fluctuations here, the velocity components may be obtained by their inclusion in the realization matrix $\hat{\mathbf{G}}$ in Eq. (21), in a procedure corresponding to extended POD [62]. Near-wall pressure structures (left frames of Fig. 12) and the associated quasistreamwise vortices peak at $y^+ \approx 35$, 20, and 40 for the $\tilde{\mathbf{\Psi}}_p$, $\mathbf{U}$, and $\mathbf{U}^{\nu_T}$ modes, respectively. The quasistreamwise vortices for the SPOD ($\tilde{\mathbf{\Psi}}_p$) and resolvent ($\mathbf{U}$) modes have clockwise rotation associated with negative (blue) pressure, whereas counterclockwise vortices are associated with positive (red) pressure values. Although the position of quasistreamwise vortices (i.e., the phase with respect to pressure fluctuations) is correct for the resolvent mode, the vortices are more concentrated around the critical layer, as usual for resolvent modes with molecular viscosity [56]. This mode is similar to that shown by Abreu *et al.* [32], who employed an L_2 norm accounting for the three velocity components (kinetic energy norm) to extract the SPOD and resolvent modes at $(\lambda_x^+, \lambda_z^+, \lambda_t^+) \approx (1000, 100, 100)$, i.e., the wave number–frequency triplet of the premultiplied spectrum peak for the near-wall structures. The large-scale structures span almost the entire channel half-height and have a dynamics similar to that observed for the near-wall structures. For the SPOD and resolvent modes, the quasistreamwise vortices have support at $y \approx 0.40$ and 0.35, respectively. The eddy-viscosity resolvent mode, on the other hand, peaks at $y \approx 0.15$ and also shows the quasistreamwise vortices in the intersection between regions of high and low pressure.

The pressure modes for the spanwise-coherent structures are shown in Fig. 13. First, second and third columns correspond to the SPOD ($\tilde{\mathbf{\Psi}}_p$), resolvent ($\mathbf{U}$), and eddy-viscosity resolvent ($\mathbf{U}^{\nu_T}$) modes, respectively. The pressure structures span the channel half-height. Moreover, for the three modal decompositions, regions of low pressure are associated with clockwise vortices, whereas for the regions of high pressure, the vortices rotate in the counterclockwise direction. Near the wall, the pressure component for the $\mathbf{U}^{\nu_T}$ modes displays a slight inclination towards the right direction, which is not observed for the $\tilde{\mathbf{\Psi}}_p$ and $\mathbf{U}$ modes. Similarly to near-wall and large-scale structures, both resolvent modes display a fairly close agreement with the SPOD mode taken from the DNS.

Figures 14 and 15 show the second resolvent and SPOD modes in the same fashion as the Figs. 12 and 13. We observe that the second mode now shows a pair of structures along y, in phase opposition. This is similar to what is observed for corresponding velocity modes [32]. The resolvent modes reproduce the phase opposition observed in the SPOD mode but with a sharper jump that contrasts with the smoother phase change along y in the SPOD mode. The second modes appear to be related to a similar mechanism in the leading flow response, this time leading to structures in phase opposition along y.

B. Comparison to velocity modes

We now compare some features of the observed pressure structures with modes obtained considering the more usual metrics related to velocity fluctuations. Figures 16 and 17 display the SPOD ($\tilde{\mathbf{\Psi}}_{TKE}$), resolvent ($\mathbf{U}_{TKE}$), and eddy-viscosity resolvent ($\mathbf{U}^{\nu_T}_{TKE}$) modes for the near-wall and large-scale structures and spanwise-coherent structure, respectively, defining operators $\mathbf{C}$ [Eq. (9)]
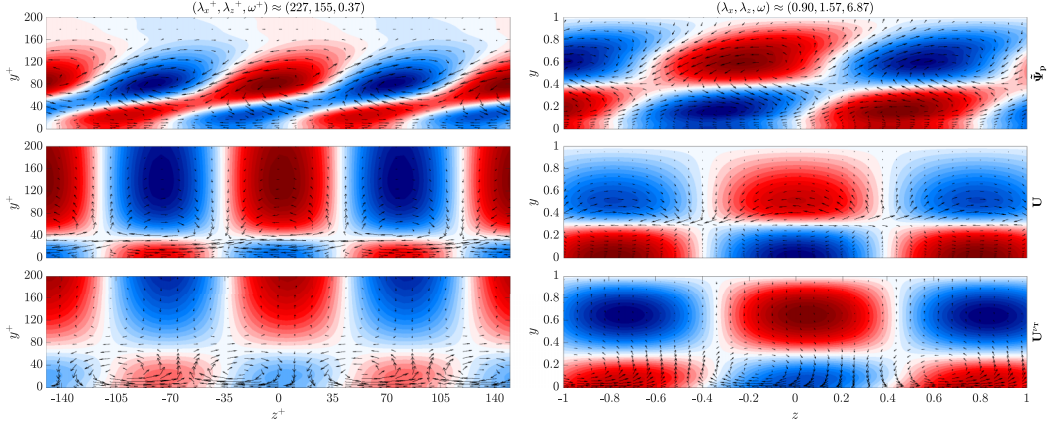
FIG. 14. Pressure near-wall (left frames) and large-scale (right frames) structures modes for the $\mathrm{Re}_\tau \approx 550$ simulation. Rows (from top to bottom): Second SPOD ($\tilde{\boldsymbol{\Psi}}_p$), resolvent ($\boldsymbol{U}$), and eddy-viscosity resolvent ($\boldsymbol{U}^{\nu_T}$) modes. See the comments in the caption of Fig. 12.

and $\boldsymbol{W}$ [Eq. (22)] to target the turbulent kinetic energy (TKE) as

$$
\boldsymbol{C} = \begin{bmatrix} \boldsymbol{I} & \boldsymbol{Z} & \boldsymbol{Z} & \boldsymbol{Z} \\ \boldsymbol{Z} & \boldsymbol{I} & \boldsymbol{Z} & \boldsymbol{Z} \\ \boldsymbol{Z} & \boldsymbol{Z} & \boldsymbol{I} & \boldsymbol{Z} \\ \boldsymbol{Z} & \boldsymbol{Z} & \boldsymbol{Z} & \boldsymbol{Z} \end{bmatrix},
\tag{30}
$$

and

$$
\boldsymbol{W} = \begin{bmatrix} \boldsymbol{K}_p & \boldsymbol{Z} & \boldsymbol{Z} & \boldsymbol{Z} \\ \boldsymbol{Z} & \boldsymbol{K}_p & \boldsymbol{Z} & \boldsymbol{Z} \\ \boldsymbol{Z} & \boldsymbol{Z} & \boldsymbol{K}_p & \boldsymbol{Z} \\ \boldsymbol{Z} & \boldsymbol{Z} & \boldsymbol{Z} & \boldsymbol{Z} \end{bmatrix}.
\tag{31}
$$

The obtained TKE-targeted structures display overall similarities the pressure-targeted structures (Figs. 12 and 13). The TKE-SPOD modes are more inclined towards the right direction with respect to their pressure counterpart. While the TKE and pressure resolvent modes are very similar, likely due to the low-rank nature of the linearized system, the eddy-viscosity resolvent has different modes, with pressure structures with strong variations near the wall, in contrast with the smoother SPOD modes. Moreover, the spanwise-coherent structure using pressure and TKE metrics are almost identical, except for the eddy-viscosity resolvent mode that has a near wall behavior in contrast
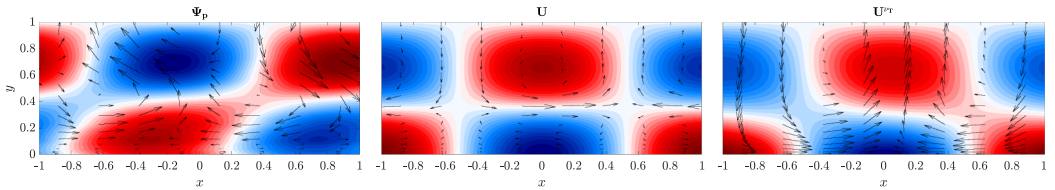

FIG. 15. Pressure spanwise-coherent structures for the $\mathrm{Re}_\tau \approx 550$ simulation. Frames (from left to right): Second SPOD ($\tilde{\boldsymbol{\Psi}}_p$), resolvent ($\boldsymbol{U}$), and eddy-viscosity resolvent ($\boldsymbol{U}^{\nu_T}$) modes. See the comments in the caption of Fig. 12.
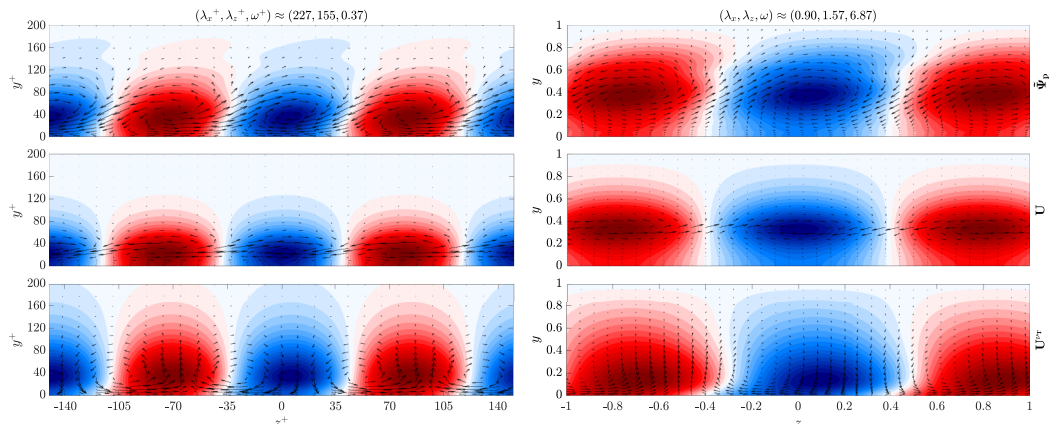
FIG. 16. TKE near-wall (left frames) and large-scale (right frames) structures modes for the $Re_\tau \approx 550$ simulation. See the comments in the caption of Fig. 12.

with the SPOD mode. We observe that the use of the pressure as a single variable determining the level of agreement simplifies the modeling task, as a single scalar SPOD mode must be matched by linearized models.

To explore the different mechanisms leading to pressure and velocity responses, Fig. 18 shows the divergence of the resolvent forcing first mode evaluated with (bottom row) and without the eddy-viscosity model (top row) for the three studied structures, i.e., near-wall, large-scale, and spanwise coherent structures (columns, from left to right). Differently from the forcing modes obtained with a TKE energy norm, which are solenoidal or incompressible [44], the divergence of the forcing when accounting for a pressure energy norm is not zero. Thus, there are additional mechanisms leading to pressure fluctuations, related to the nonzero divergence of nonlinear terms.

C. Parametric comparison between resolvent and SPOD modes

To assess a quantitative comparison between the SPOD and resolvent pressure modes, it is possible to project the first SPOD mode onto the optimal resolvent for a combination (α, β, ω) in the same fashion as Abreu *et al.* [35], i.e.,

$$\Gamma = \left| \frac{\langle a, b \rangle}{||a|| ||b||} \right|, \tag{32}$$

where Γ is the normalized projection, with $\Gamma \in [0, 1]$, a and b are two modes to be compared, $\langle \cdot, \cdot \rangle$ denotes the L_2 inner product, $|| \cdot ||$ indicates the L_2 norm, and $| \cdot |$ indicates absolute value. It is important to remark that $\Gamma = 0$ and $\Gamma = 1$ indicate that the vectors are orthogonal and perfectly
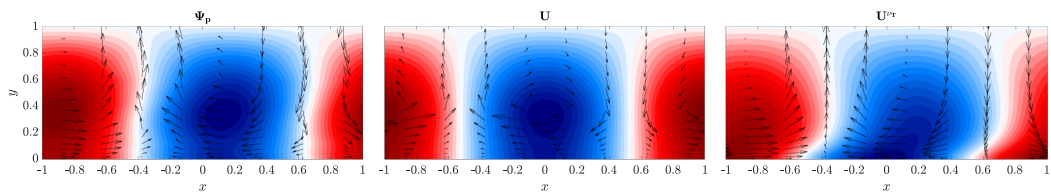

FIG. 17. TKE spanwise-coherent structures for the $Re_\tau \approx 550$ simulation. See the comments in the caption of Fig. 13.
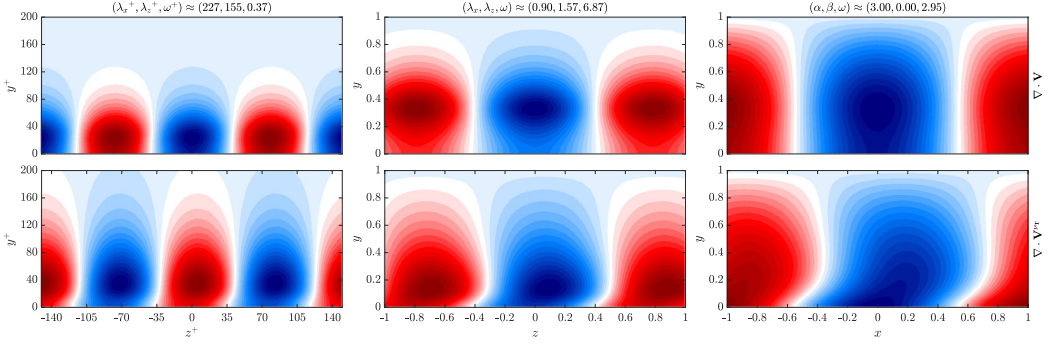
FIG. 18. Divergence of the first forcing mode (top row) and eddy-viscosity forcing mode (bottom row) for the $Re_\tau \approx 550$ case. Frames (from left to right): Near-wall, large-scale, and spanwise coherent structures.

aligned, respectively. Here $\boldsymbol{a} = \tilde{\boldsymbol{\psi}}_1$, i.e., the first SPOD pressure mode, and $\boldsymbol{b} = \boldsymbol{U}_1$ or $\boldsymbol{b} = \boldsymbol{U}_1^{\nu_T}$, i.e., the optimal resolvent or eddy-viscosity resolvent pressure mode.

Figures 19 and 20 exhibit the projection coefficients for the $Re_\tau \approx 180$ and 550 cases, respectively, for the temporal frequencies of the near-wall, large-scale, and spanwise-coherent structures. The coefficients were evaluated for all wave numbers contained in the database and are shown in contours in the figure; top row for the resolvent operator and bottom row for the eddy-viscosity resolvent operator. The cross markers on each frame indicate the wave-number pair correspondent to the structure's energy peak. Overall, for the frequency corresponding to near-wall structures, high projection coefficient levels are observed for low streamwise and spanwise wavelengths. For the large-scale frequency, the band of high level coefficient levels is enlarged, but the higher levels are still attained for the lower wavelengths. Regarding the characteristic frequency of spanwise coherent structures, the normalized projection levels are approximately homogeneous in the wave-number space, despite a few regions where lower and higher levels can be observed. However, for both Reynolds numbers, note the molecular-viscosity resolvent leads to high projection coefficients in the high-α–low-β region, while the eddy-viscosity formulation leads to higher coefficients in the low-α–high-β region. Yet, for the $Re_\tau \approx 550$ case and considering molecular-viscosity resolvent (top-right frame of Fig. 20), there is a gap in the projection coefficient around the $2 \leqslant \alpha \leqslant 4$ and
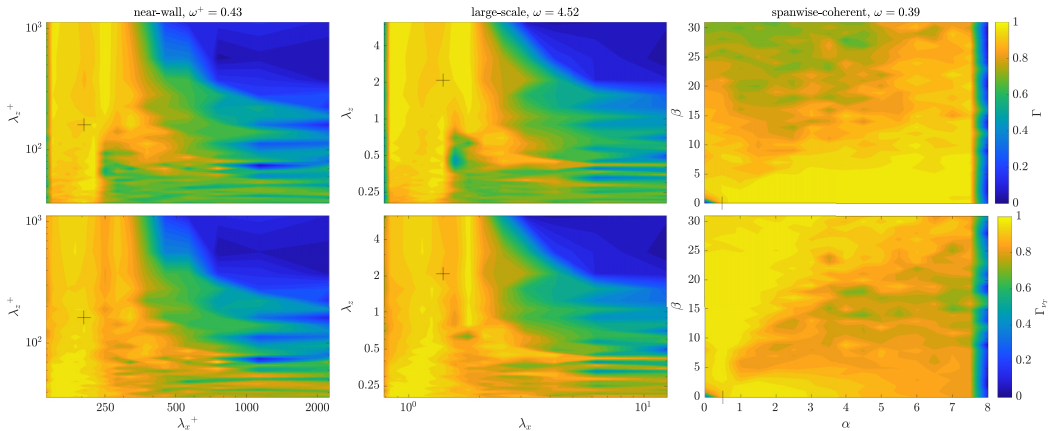

FIG. 19. Projection coefficients (pressure norm) of the first SPOD mode on the first resolvent (top row) and eddy-viscosity resolvent (bottom row) modes for the $Re_\tau \approx 180$ case.
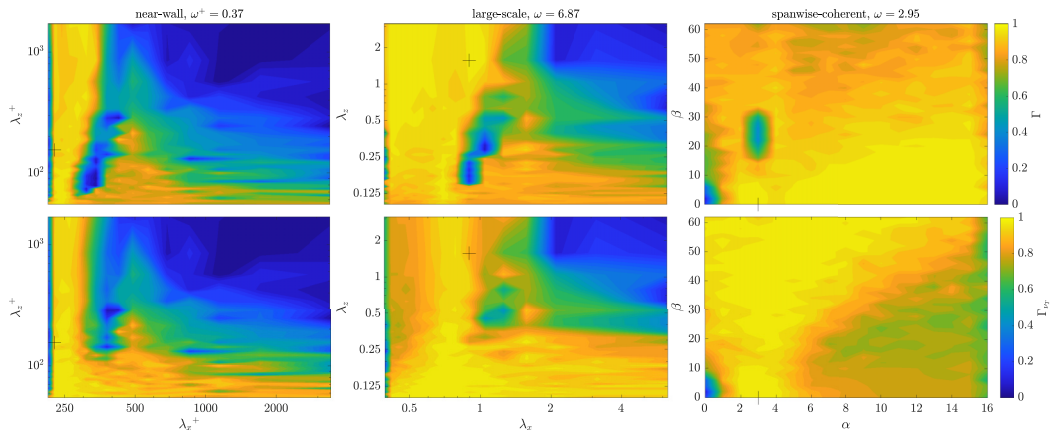
FIG. 20. Projection coefficients (pressure norm) of the first SPOD mode on the first resolvent (top row) and eddy-viscosity resolvent (bottom row) modes for the $\mathrm{Re}_\tau \approx 550$ case.

$20 \leqslant \beta \leqslant 30$ regions, which does not occur for the eddy-viscosity resolvent nor for the $\mathrm{Re}_\tau \approx 180$ case and both resolvent formulations. Overall, besides the considerations above, for the three considered frequencies, there is no clear advantage for resolvent models with or without the eddy viscosity, with both approaches having similar parameter ranges with good agreement with the leading SPOD modes.

Tables III and IV display the projection coefficients for the $\mathrm{Re}_\tau \approx 180$ and 550 cases, respectively, for the near-wall, large-scale, and spanwise-coherent structures (cross markers in Fig. 20). It is observed that indeed the pressure SPOD first modes project very well onto the resolvent and eddy-viscosity resolvent optimal pressure modes of the three selected structures, especially the near-wall and spanwise-coherent structures, with $\Gamma \geqslant 0.94$. As commented before, there is no clear advantages for one of the resolvent models.

Figures 21 and 22 show the projection coefficients using the TKE norm instead of the pressure norm, as in Abreu *et al.* [32,35]. In comparison to the pressure norm counterpart, Figs. 19 and 20, the region of high projection coefficient values is smaller for the three studied structures. Regarding the near-wall and spanwise-coherent structures, higher values are obtained only for the smaller streamwise wavelengths, whereas for the spanwise-coherent structure, the projection coefficient is more uniformly spread along the streamwise and spanwise wavelength space, as for the pressure norm. The differences between the resolvent and the eddy-viscosity resolvent when using the TKE norm are qualitatively the same as when using the pressure norm, i.e., overall lower projection levels are attained for the eddy-viscosity resolvent, although the region comprising low spanwise wave numbers shows higher projection coefficient levels for higher streamwise wave numbers.

TABLE III. Projection coefficients for the pressure modes and $\mathrm{Re}_\tau \approx 180$ case.

Projection	Near-wall structure $(\lambda_x{}^+, \lambda_z{}^+, \omega^+) \approx (204, 161, 0.43)$	Large-scale structure $(\lambda_x, \lambda_z, \omega) \approx (1.40, 2.09, 4.52)$	Spanwise-coherent structure $(\alpha, \beta, \omega) \approx (0.50, 0.00, 0.39)$
Γ	0.94	0.91	0.97
Γ_{ν_T}	0.95	0.94	0.96

TABLE IV. Projection coefficients for the pressure modes and $Re_\tau \approx 550$ case.

	Near-wall structure	Large-scale structure	Spanwise-coherent structure
Projection	$(\lambda_x^+, \lambda_z^+, \omega^+) \approx (227, 155, 0.37)$	$(\lambda_x, \lambda_z, \omega) \approx (0.90, 1.57, 6.87)$	$(\alpha, \beta, \omega) \approx (3.00, 0.00, 2.95)$
Γ	0.96	0.89	0.99
Γ_{ν_T}	0.98	0.97	0.98

V. ROLE OF DIFFERENT FORCING COMPONENTS

A further effort to explore how the forcing leads to the observed pressure statistics is pursued in this section. In order to do so, let us consider the effect of the input sub-blocks (forcing CSD) on the output (pressure CSD). The CSD F can be interpreted as a sum of sub-blocks (F_{ij}), with each sub-block accounting for a forcing component, i.e.,

$$F = F_{xx} + F_{xy} + F_{xz} + F_{yy} + F_{yx} + F_{yz} + F_{zz} + F_{zx} + F_{zy}, \qquad (33)$$

where the subscripts i and j in the F_{ij} sub-block notation indicate the streamwise (x), wall-normal (y) and/or spanwise (z) forcing components. Note that because input F is Hermitian for $i \neq j$, we will consider F_{ij} and F_{ji} combined.

Figures 23 and 24 show the output s_{pp} as a function of the inputs F_{ij} and F for $Re_\tau \approx 180$ and 550 simulations, respectively. The left frames of the figures correspond to the near-wall structures, whereas the middle and right frames denote large-scale and spanwise-coherent structures, respectively. A first observation is that using the full forcing statistics F leads to a nearly exact recovery of the full response statistics S from the DNS. This provides further validation of the present database.

The forcing CSD terms considering $i = j$ provide positive contribution of pressure PSD. For the near-wall (of both cases) and large-scale (of the $Re_\tau \approx 180$ case) structures, the F_{xy} and F_{yz} terms have a slightly negative contribution to the pressure output, in a region very close to the wall, whereas the F_{xz} terms provide a slightly positive contribution. For the large-scale structure for the $Re_\tau \approx 550$ channel, the F_{xy} and F_{yz} terms have a negative contribution at $y \approx 0.3$, whereas the F_{xz} term has a positive contribution around this same wall-normal position. Regarding the spanwise-coherent structures, all terms related to the spanwise forcing presented no contribution to the output,
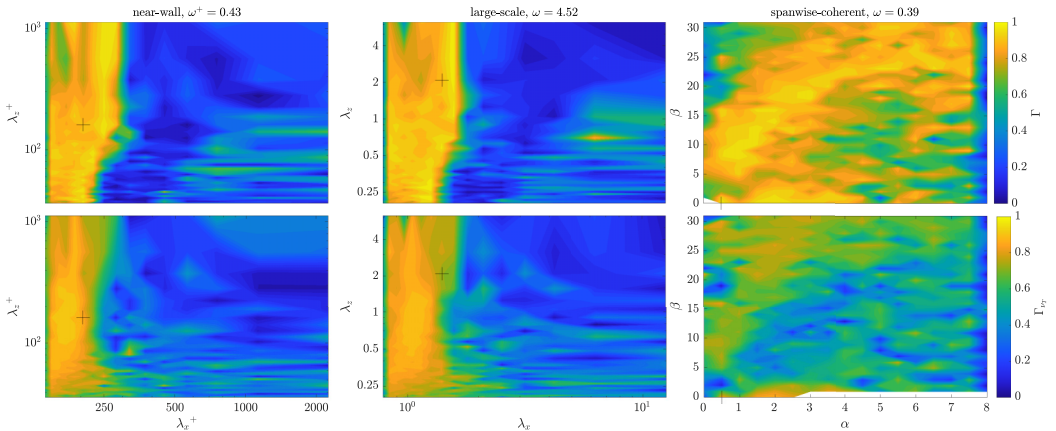

FIG. 21. Projection coefficients (TKE norm) of the first SPOD mode on the first resolvent (top row) and eddy-viscosity resolvent (bottom row) modes for the $Re_\tau \approx 180$ case.
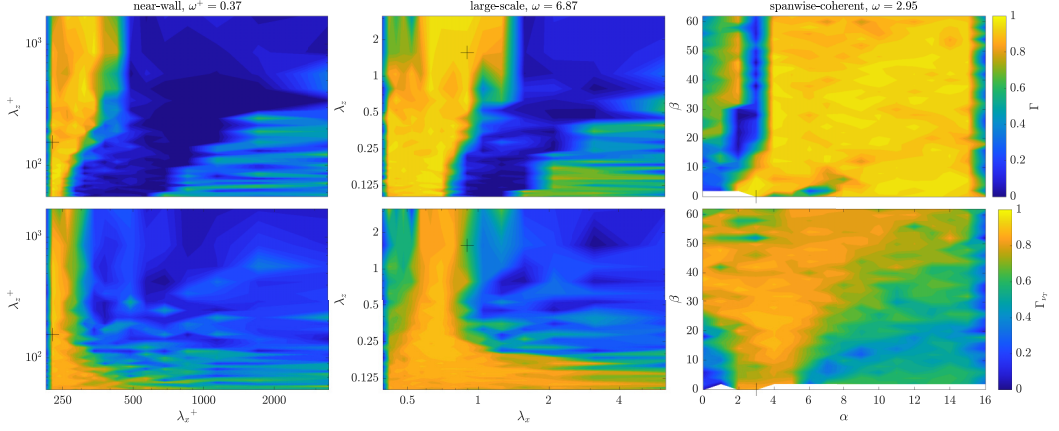
FIG. 22. Projection coefficients (TKE norm) of the first SPOD mode on the first resolvent (top row) and eddy-viscosity resolvent (bottom row) modes for the $\mathrm{Re}_\tau \approx 550$ case.

as expected; the pressure structures are thus two dimensional, resulting solely from streamwise and wall-normal forcing.

The scenario presented here contrasts with that of Morra *et al.* [44], who studied the contributions of the input CSD sub-blocks on the streamwise velocity component CSD output for near-wall and large-scale structures. Morra *et al.* [44] showed that when $i = j$, the CSD terms positively contribute to the streamwise velocity output, whereas the $i \neq j$ terms mostly presented a negative contribution. The authors observed that both positive and negative contributions have approximately the same amplitude levels, which lead to cancellations in the output if the full input (forcing) CSD is considered. On the other hand, overall, in the present study the positive contributions of the input CSD sub-blocks have higher amplitudes than the negative contributions. Therefore, when all input CSD terms are considered, a positive pressure output is obtained, with higher amplitude than those observed if only isolated input CSD sub-blocks are considered, in a mostly constructive interference. Differently from Morra *et al.* [44], it seems that for the pressure component the input CSD off-diagonal terms ($i \neq j$) do not play a leading role, at least for the near-wall structures, as the magnitude of such terms is much smaller than that of the diagonal terms ($i = j$). The exceptions seem to occur for the large-scale and spanwise-coherent structures at $\mathrm{Re}_\tau \approx 550$ (middle and right frames of Fig. 24), for which the $\boldsymbol{F}_{xy}$ term has a large negative amplitude that significantly contributes for the output when considering the full forcing CSD. Such characteristics of nonlinear
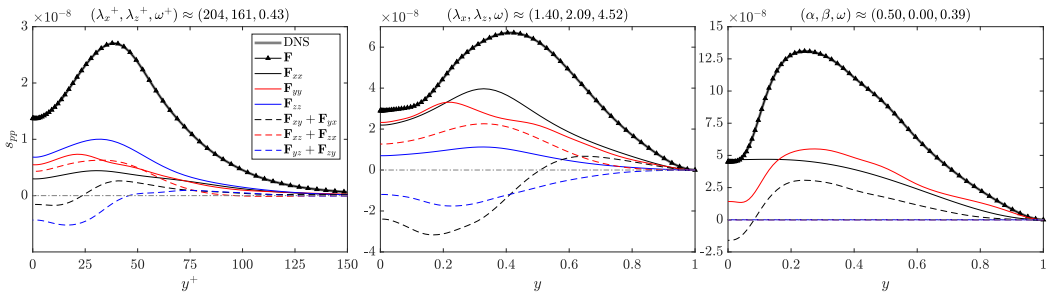

FIG. 23. Pressure component response $\boldsymbol{S} = \boldsymbol{H}\boldsymbol{F}_{ij}\boldsymbol{H}^\dagger$ from sub-blocks $\boldsymbol{F}_{ij}$ for $\mathrm{Re}_\tau \approx 180$. Solid lines: Response from sub-blocks $\boldsymbol{F}_{ii}$. Dashed lines: Response from sub-blocks $\boldsymbol{F}_{ij}$ with $i \neq j$. Triangles: Response from full forcing CSD. Gray thick line: Response from DNS. Frames, from left to right: Near-wall, large-scale, and spanwise-coherent structures, respectively.
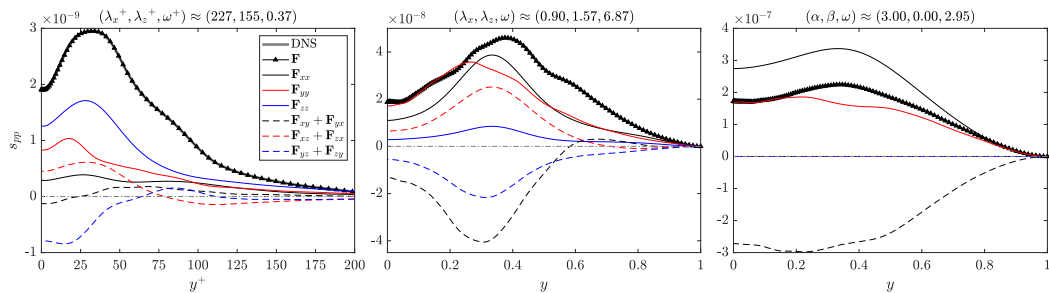
FIG. 24. Pressure component response $S = HF_{ij}H^{\dagger}$ from sub-blocks F_{ij} for $Re_{\tau} \approx 550$. See the comments in the caption of Fig. 23.

terms suggest that a simpler forcing model may be possible if one is interested in pressure structures. The lower level of destructive interference also helps understanding the good performance of both resolvent modes in predicting the leading SPOD modes.

VI. CONCLUSIONS

Pressure fluctuations in turbulent channel flows at $Re_{\tau} \approx 180$ and 550 were studied in this paper, using results from DNSs. The simulation were validated against literature results and good agreement was achieved for the rms [54] and one-dimensional power spectra in the streamwise and spanwise directions [11,13]. The two databases allowed extraction of dominant pressure structures, analyzed using wave-number spectra and SPOD. SPOD modes were then compared to results from resolvent analysis in order to evaluate the potential of linearized models to represent such pressure structures.

Peak wave number–frequency combinations were selected based on spectra without and with premultiplication for planes at the channel wall ($y = 0$) and at $y \approx 0.5$. Three characteristic structures were studied in more detail, corresponding to near-wall, large-scale, and spanwise-coherent ($\beta = 0$) structures. The premultiplied spectra for the wall plane (near-wall structures) showed a peak that collapsed in inner units at $(\lambda_x^+, \lambda_z^+, \omega^+) \approx (200, 160, 0.4)$ for both Reynolds numbers. Regarding the large-scale structures ($y \approx 0.5$), the premultiplied spectra peak do not collapse for the two Reynolds numbers.

Comparisons among the pressure SPOD and resolvent modes, with and without the inclusion of an eddy-viscosity model, were performed. Both resolvent and eddy-viscosity resolvent modes displayed good agreement with the SPOD modes. Such results can be explained by a clearer low-rank nature of the pressure SPOD modes, with a strong dominance of the leading mode for the wave number–frequency combinations presently studied. As the resolvent modes comprise quasistreamwise (for near-wall and large-scale structures) and spanwise vortices with pressure peaking at vortex centers, the analysis shows that forcing such vortices is the dominant mechanism leading to pressure fluctuations in turbulent channel flows. Differently from works that focused on velocity components [43,44], the eddy-viscosity resolvent pressure modes does not show a clear advantage in terms of better agreement with the SPOD pressure modes.

The analysis of the nonlinear terms and their individual impacts on the pressure output reveals that the forcing terms have a predominantly constructive contribution to the output. Moreover, with exception of the large-scale structures of the $Re_{\tau} \approx 550$ channel, the off-diagonal terms of the forcing CSD [see expression (33)], are less important than the diagonal terms to obtain a good prediction of the pressure outputs.

In a previous study by our group, which employed a resolvent-based formulation to estimate the flow field from wall measurements [63], we noted that pressure structures were more accurate predicted than the velocity components, especially for distances far from the wall, with less

dependence on the details of the forcing considered in the linearized model. The present results show a more marked low-rank behavior of pressure fluctuations, which may explain the ability of resolvent models to predict or estimate pressure structures. We believe that the results shown in this paper reinforces the need for proper modeling the color of forcing (nonlinear) terms when the problem is cast in the input-output framework, albeit with a lower effect of forcing color on pressure fluctuations compared to velocity components. Moreover, the resolvent operator is a valuable asset to study the most energetic pressure structures and obtain relevant amplification mechanisms for turbulent pressure fluctuations.

APPENDIX: COMPLEMENTARY RESULTS FOR THE $Re_\tau \approx 180$ SIMULATION

Figure 25 show the spectra evaluated with premultiplication. The $\lambda_x{}^+$ peak value agrees with previous studies [13,16]. At a distance characteristic of large-scale motions (right frame of Fig. 25), the peak is located at $(\lambda_x, \lambda_z) \approx (1.40, 2.09)$. The spectra without premultiplication are shown in Fig. 26. At both the wall and $y \approx 0.5$, the spectra peak at $(\alpha, \beta) = (0.5, 0)$, showing spanwise elongated pressure structures. A peak of the pressure spectrum for $\beta \to 0$ was also documented in Yang and Yang [14].

The pressure and forcing components PSDs are shown in Fig. 27 for the near-wall and large-scale structures. For the near-wall structures, the pressure component PSD peaks at $c^+ \approx 14$ ($\omega^+ \approx 0.43$), with spatial support around $y^+ \approx 38$, whereas for the large structures, such peak is located at $c^+ \approx 16$ ($\omega \approx 4.52$), with support $y \approx 0.42$. These peaks arise along the critical layer, shown in the plots with dashed lines. The ω^+ peak value is roughly in agreement with previous results [12,13]. Regarding the streamwise forcing component PSD, the near-wall and large-scale structures peak at $c^+ \approx 12.5$, with support close to the wall, at $y^+ \approx 10$.

Figure 28 shows the pressure (right frame) and streamwise forcing (left frame) components PSDs for the peak at $(\alpha, \beta) = (0.5, 0)$, which is present for the power spectra without premultiplication (Fig. 26). Both PSDs peak at $c^+ \approx 12.5$, although for the pressure component the peak has support
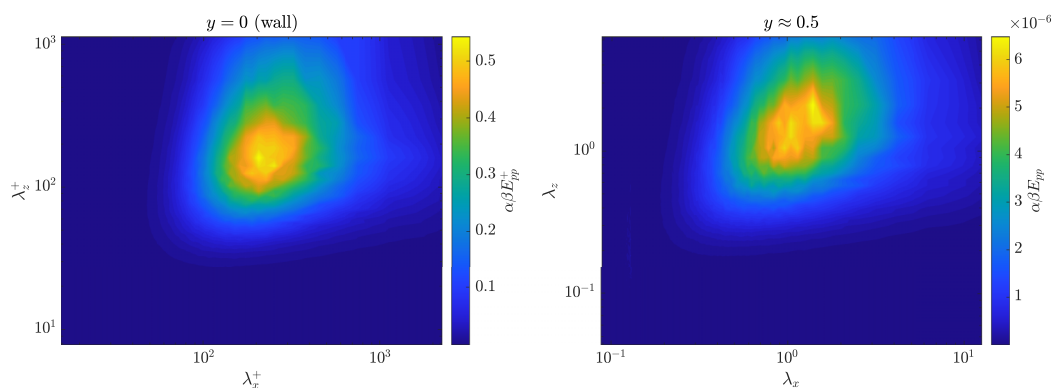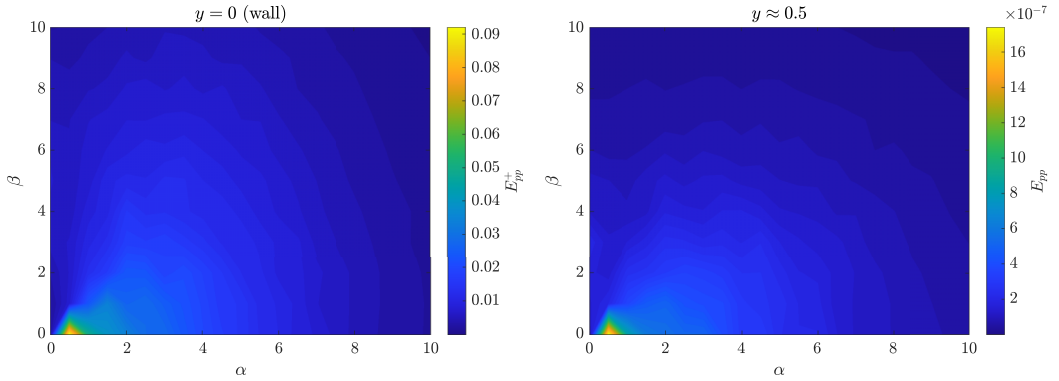

FIG. 25. Premultiplied energy spectra for $Re_\tau \approx 180$ simulation.

FIG. 26. Energy spectra for $Re_\tau \approx 180$ simulation.

at $y^+ \approx 44$, whereas for the streamwise forcing component the support is much closer to the wall, at $y^+ \approx 6.5$.

The SPOD eigenvalues and the resolvent eigenvalues are shown in Figs. 29 and 30. Similar results as those obtained for the $Re_\tau \approx 550$ simulation are observed for the $Re_\tau \approx 180$ simulation, i.e., the SPOD eigenvalue and the resolvent gains without the eddy viscosity present low-rank behavior, whereas the eddy-viscosity resolvent gains do not.

Low-rank representations of the pressure PSD using the first resolvent mode, without and with eddy viscosity, are depicted in Figs. 31 and 32. As for the $Re_\tau \approx 550$ case, the low-rank model
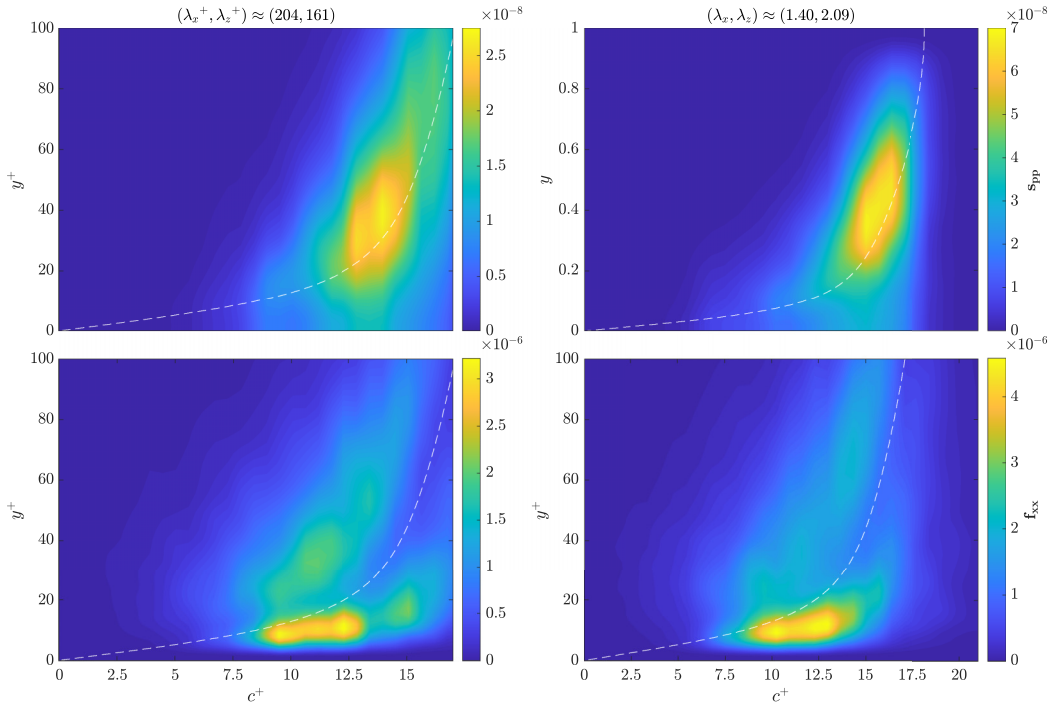

FIG. 27. PSDs for $Re_\tau \approx 180$ simulation. Left frames: Near-wall structures. Right frames: large-scale structures. Top frames: Pressure component (s_{pp}). Bottom frames: Streamwise forcing component (f_{xx}). Dashed lines denote the critical layer.
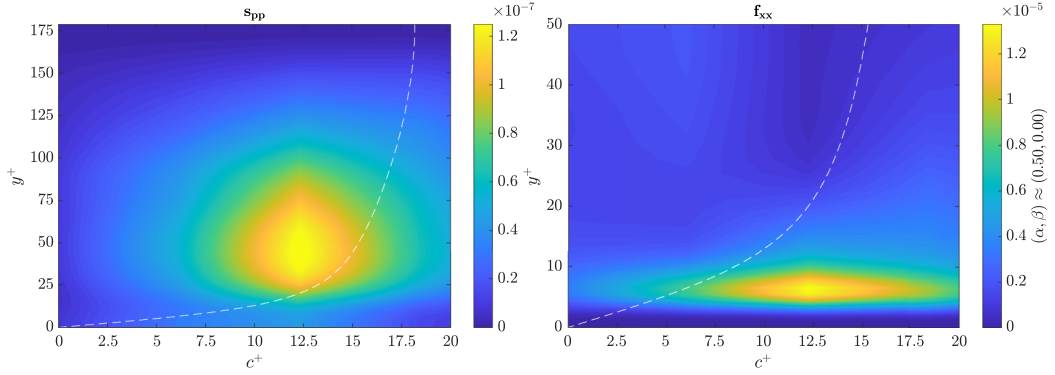
FIG. 28. PSDs for $\mathrm{Re}_\tau \approx 180$ simulation and spanwise-coherent structure, i.e., $(\alpha, \beta) = (0.5, 0)$. Right frame: Pressure component (s_{pp}). Left frame: Streamwise forcing component (f_{xx}). Dashed lines denote the critical layer.
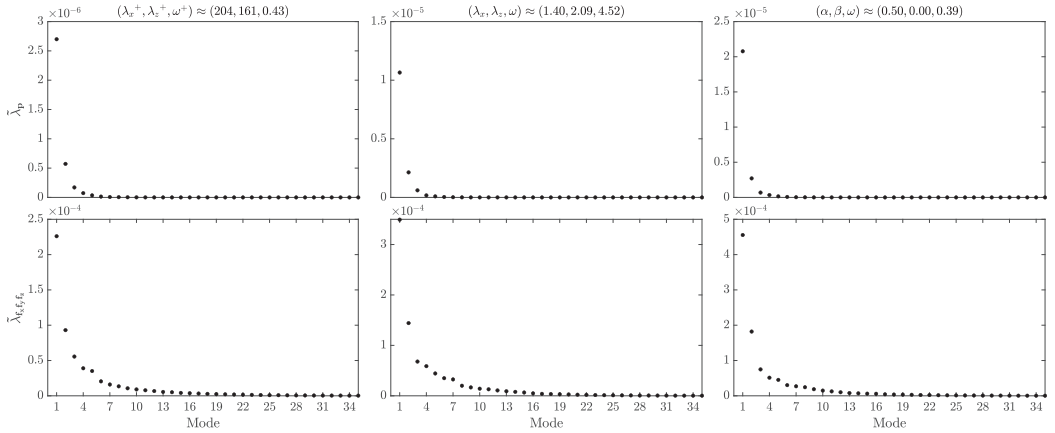

FIG. 29. SPOD eigenvalues employing the pressure (top frames) and forcing (bottom frames) modes for the $\mathrm{Re}_\tau \approx 180$ simulation. See the comments in the caption of Fig. 8.
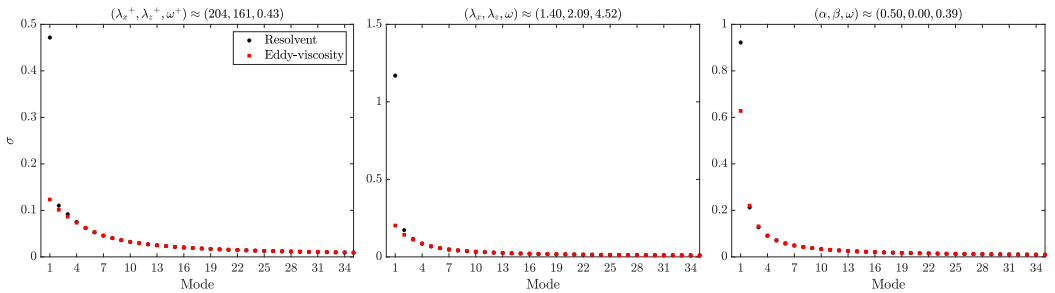

FIG. 30. Resolvent gains employing the pressure weighing for the $\mathrm{Re}_\tau \approx 180$ simulation. See the comments in the caption of Fig. 9.
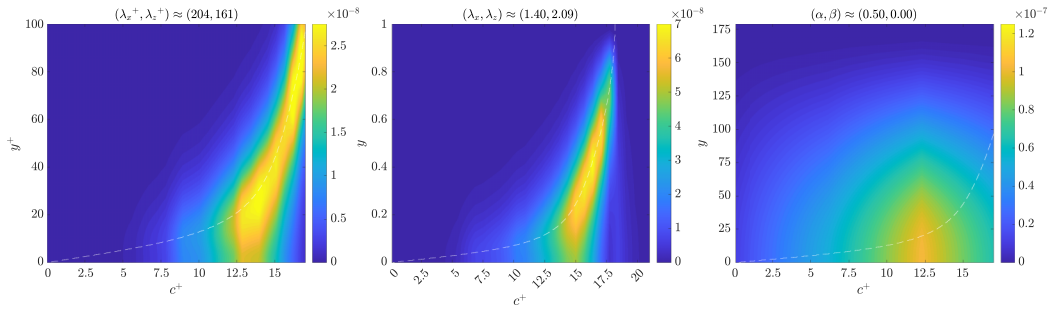
FIG. 31. Pressure component PSD low-rank resolvent reconstruction (first mode) for the $\mathrm{Re}_\tau \approx 180$ simulation. See the comments in the caption of Fig. 10.
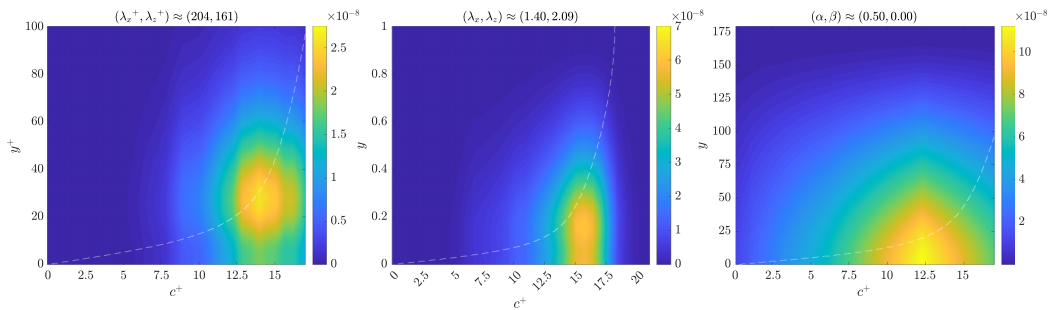

FIG. 32. Pressure component PSD low-rank eddy-viscosity resolvent reconstruction (first mode) for the $\mathrm{Re}_\tau \approx 180$ simulation. See the comments in the caption of Fig. 10.
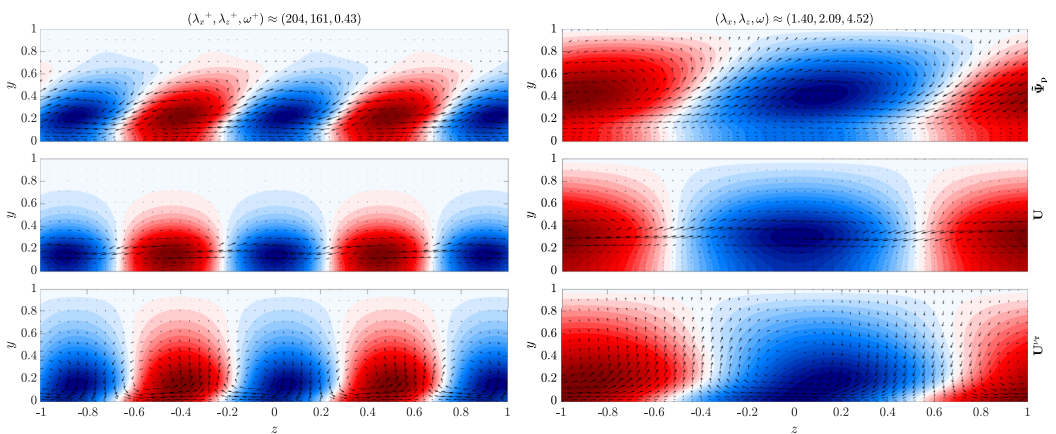

FIG. 33. Pressure near-wall (left frames) and large-scale (right frames) structures modes for the $\mathrm{Re}_\tau \approx 180$ simulation. See the comments in the caption of Fig. 12.
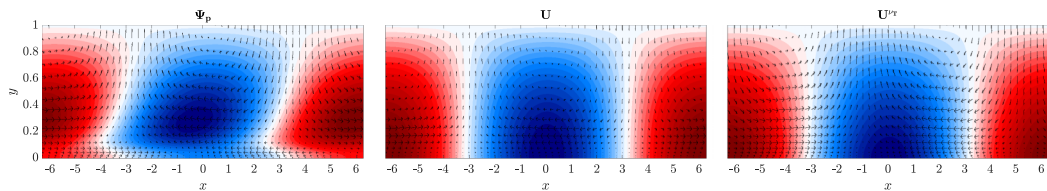
FIG. 34. Pressure spanwise-coherent structures for the $\mathrm{Re}_\tau \approx 180$ simulation. See the comments in the caption of Fig. 13.

was able to capture the main features of the DNS PSD, especially for the resolvent without eddy viscosity.

Near-wall, large-scale, and spanwise-coherent pressure modes obtained through SPOD and resolvent analysis are shown in Figs. 33 and 34. The results are similar to those obtained for the $\mathrm{Re}_\tau \approx 550$ simulation (Figs. 12 and 13). The streamwise component of the $\tilde{\boldsymbol{\Psi}}_p$ (SPOD) modes are inclined to the right for $y \geqslant 0.1$, whereas for the $\boldsymbol{U}$ (resolvent) modes the regions of positive and negative pressure are normal to the wall. On the other hand, the streamwise component of the $\boldsymbol{U}^{\nu_T}$ (eddy-viscosity resolvent) modes are inclined to the left close to the wall, up to $y \leqslant 0.25$, whereas for $y > 0.25$, they are slightly inclined to the right. Such feature is evident for the near-wall and large-scale structures and at some extent for the spanwise-coherent structure.

[1] S. Lee, L. Ayton, F. Bertagnolio, S. Moreau, T. P. Chong, and P. Joseph, Turbulent boundary layer trailing-edge noise: Theory, computation, experiment, and application, Prog. Aerosp. Sci. **126**, 100737 (2021).

[2] W. W. Willmarth, Pressure fluctuations beneath turbulent boundary layers, Annu. Rev. Fluid Mech. **7**, 13 (1975).

[3] G. Schewe, On the structure and resolution of wall-pressure fluctuations associated with turbulent boundary-layer flow, J. Fluid Mech. **134**, 311 (1983).

[4] T. M. Farabee and M. J. Casarella, Spectral features of wall pressure fluctuations beneath turbulent boundary layers, Phys. Fluids **3**, 2410 (1991).

[5] M. K. Bull, Wall-pressure fluctuations beneath turbulent boundary layers: Some reflections on forty years of research, J. Sound Vib. **190**, 299 (1996).

[6] B. Arguillat, D. Ricot, G. Robert, and C. Bailly, Measured wavenumber: Frequency spectrum associated with acoustic and aerodynamic wall pressure fluctuations, J. Acoust. Soc. Am. **128**, 1647 (2010).

[7] S. P. Gravante, A. M. Naguib, C. E. Wark, and H. M. Nagib, Characterization of the pressure fluctuations under a fully developed turbulent boundary layer, AIAA J. **36**, 1808 (1998).

[8] Y. Tsuji, J. H. M. Fransson, P. H. Alfredsson, and A. V. Johansson, Pressure statistics and their scaling in high-Reynolds-number turbulent boundary layers, J. Fluid Mech. **585**, 1 (2007).

[9] J. C. Klewicki, P. J. A. Priyadarshana, and M. M. Metzger, Statistical structure of the fluctuating wall pressure and its in-plane gradients at high Reynolds number, J. Fluid Mech. **609**, 195 (2008).

[10] J. Kim, P. Moin, and R. Moser, Turbulence statistics in fully developed channel flow at low Reynolds number, J. Fluid Mech. **177**, 133 (1987).

[11] H. Choi and P. Moin, On the space-time characteristics of wall-pressure fluctuations, Phys. Fluids **2**, 1450 (1990).

[12] Z. W. Hu, C. L. Morfey, and N. D. Sandham, Wall pressure and shear stress spectra from direct simulations of channel flow, AIAA J. **44**, 1541 (2006).

[13] S. Anantharamu and K. Mahesh, Analysis of wall-pressure fluctuation sources from direct numerical simulation of turbulent channel flow, J. Fluid Mech. **898**, A17 (2020).

[14] B. Yang and Z. Yang, On the wavenumber–frequency spectrum of the wall pressure fluctuations in turbulent channel flow, J. Fluid Mech. **937**, A39 (2022).

[15] J. Kim, On the structure of pressure fluctuations in simulated turbulent channel flow, J. Fluid Mech. **205**, 421 (1989).

[16] R. L. Panton, M. Lee, and R. D. Moser, Correlation of pressure fluctuations in turbulent wall layers, Phys. Rev. Fluids **2**, 094604 (2017).

[17] A. S. Sharma and B. J. McKeon, On coherent structure in wall turbulence, J. Fluid Mech. **728**, 196 (2013).

[18] C. Cossu and Y. Hwang, Self-sustaining processes at all scales in wall-bounded turbulent shear flows, Phil. Trans. R. Soc. A **375**, 20160088 (2017).

[19] S. Symon, S. J. Illingworth, and I. Marusic, Energy transfer in turbulent channel flows and implications for resolvent modelling, J. Fluid Mech. **911**, A3 (2021).

[20] R. Moarref, A. S. Sharma, J. A. Tropp, and B. J. McKeon, Model-based scaling of the streamwise energy density in high-Reynolds number turbulent channels, J. Fluid Mech. **734**, 275 (2013).

[21] A. Zare, M. R. Jovanović, and T. T. Georgiou, Colour of turbulence, J. Fluid Mech. **812**, 636 (2017).

[22] B. J. McKeon, The engine behind (wall) turbulence: Perspectives on scale interactions, J. Fluid Mech. **817**, P1 (2017).

[23] B. J. McKeon and A. S. Sharma, A critical-layer framework for turbulent pipe flow, J. Fluid Mech. **658**, 336 (2010).

[24] Y. Hwang and C. Cossu, Linear non-normal energy amplification of harmonic and stochastic forcing in the turbulent channel flow, J. Fluid Mech. **664**, 51 (2010).

[25] M. Luhar, A. S. Sharma, and B. J. McKeon, On the structure and origin of pressure fluctuations in wall turbulence: Predictions based on the resolvent analysis, J. Fluid Mech. **751**, 38 (2014).

[26] A. Towne, O. T. Schmidt, and T. Colonius, Spectral proper orthogonal decomposition and its relationship to dynamic mode decomposition and resolvent analysis, J. Fluid Mech. **847**, 821 (2018).

[27] O. T. Schmidt and A. Towne, An efficient streaming algorithm for spectral proper orthogonal decomposition, Comput. Phys. Commun. **237**, 98 (2019).

[28] L. Lesshafft, O. Semeraro, V. Jaunet, A. V. G. Cavalieri, and P. Jordan, Resolvent-based modeling of coherent wave packets in a turbulent jet, Phys. Rev. Fluids **4**, 063901 (2019).

[29] A. V. G. Cavalieri, P. Jordan, and L. Lesshafft, Wave-packet models for jet dynamics and sound radiation, Appl. Mech. Rev. **71**, 020802 (2019).

[30] B. F. Farrell and P. J. Ioannou, Dynamics of streamwise rolls and streaks in turbulent wall-bounded shear flow, J. Fluid Mech. **708**, 149 (2012).

[31] J. Jiménez, Near-wall turbulence, Phys. Fluids **25**, 101302 (2013).

[32] L. I. Abreu, A. V. G. Cavalieri, P. Schlatter, R. Vinuesa, and D. S. Henningson, Resolvent modelling of near-wall coherent structures in turbulent channel flow, Int. J. Heat Fluid Flow **85**, 108662 (2020).

[33] T. Ellingsen and E. Palm, Stability of linear flow, Phys. Fluids **18**, 487 (1975).

[34] M. T. Landahl, A note on an algebraic instability of inviscid parallel shear flows, J. Fluid Mech. **98**, 243 (1980).

[35] L. I. Abreu, A. V. G. Cavalieri, P. Schlatter, R. Vinuesa, and D. S. Henningson, Spectral proper orthogonal decomposition and resolvent analysis of near-wall coherent structures in turbulent pipe flows, J. Fluid Mech. **900**, A11 (2020).

[36] L. Brandt, The lift-up effect: The linear mechanism behind transition and turbulence in shear flows, Eur. J. Mech. B. Fluids **47**, 80 (2014).

[37] J. Jiménez, Coherent structures in wall-bounded turbulence, J. Fluid Mech. **842**, P1 (2018).

[38] R. D. Cess, A survey of the literature on heat transfer in turbulent tube flow, Technical Report Report 8-0529-R24, Westinghouse Research (1958).

[39] J. C. del Álamo and J. Jiménez, Linear energy amplification in turbulent channels, J. Fluid Mech. **559**, 205 (2006).

[40] G. Pujals, M. García-Villalba, C. Cossu, and S. Depardon, A note on optimal transient growth in turbulent channel flows, Phys. Fluids **21**, 015109 (2009).

[41] K. M. Butler and B. F. Farrell, Optimal perturbations and streak spacing in wall-bounded turbulent shear flow, Phys. Fluids **5**, 774 (1993).

[42] Y. Hwang and C. Cossu, Amplification of coherent streaks in the turbulent couette flow: An input–output analysis at low reynolds number, J. Fluid Mech. **643**, 333 (2010).

[43] S. Symon, A. Madhusudanan, S. J. Illingworth, and I. Marusic, Use of eddy viscosity in resolvent analysis of turbulent channel flow, Phys. Rev. Fluids **8**, 064601 (2023).

[44] P. Morra, P. A. S. Nogueira, A. V. G. Cavalieri, and D. S. Henningson, The colour of forcing statistics in resolvent analyses of turbulent channel flows, J. Fluid Mech. **907**, A24 (2021).

[45] M. R. Jovanović and B. Bamieh, Componentwise energy amplification in channel flows, J. Fluid Mech. **534**, 145 (2005).

[46] A. Towne, A. Lozando-Durán, and X. Yang, Resolvent-based estimation of space–time flow statistics, J. Fluid Mech. **883**, A17 (2020).

[47] L. N. Trefethen, *Spectral Methods in MATLAB SIAM* (Society for Industrial and Applied Mathematics, 2000).

[48] P. D. Welch, The use of Fast Fourier Transform for the estimation of power spectra: A method based on time averaging over short, modified periodograms, IEEE Trans. Audio Electroacoust. **15**, 70 (1967).

[49] G. Berkooz, P. Holmes, and J. L. Lumley, The proper orthogonal decomposition in the analysis of turbulent flows, Annu. Rev. Fluid Mech. **25**, 539 (1993).

[50] K. Taira, S. L. Brunton, S. T. M. Dawson, C. W. Rowley, T. Colonius, B. J. McKeon, O. T. Schmidt, S. Gordeyev, V. Theofilis, and L. S. Ukeiley, Modal analysis of fluid flows: An overview, AIAA J. **55**, 4013 (2017).

[51] C. Picard and J. Delville, Pressure velocity coupling in a subsonic round jet, Int. J. Heat Fluid Flow **21**, 359 (2000).

[52] J. F. Gibson, F. Reetz, S. Azimi, A. Ferraro, T. Kreilos, H. Schrobsdorff, M. Farano, A. F. Yesil, S. S. Schütz, M. Culpo, and T. M. Schneider, ChannelFlow 2.0 https://www.channelflow.ch/.

[53] E. Martini, P. Jordan, A. V. G. Cavalieri, A. Towne, and L. Lesshafft, Resolvent-based optimal estimation of transitional and turbulent flows, J. Fluid Mech. **900**, A2 (2020).

[54] J. C. del Álamo and J. Jiménez, Spectra of the very large anisotropic scales in turbulent channels, Phys. Fluids **15**, L41 (2003).

[55] T. A. Zang, On the rotation and skew-symmetric forms for incompressible flow simulations, Appl. Numer. Math. **7**, 27 (1991).

[56] P. Morra, O. Semeraro, D. S. Henningson, and C. Cossu, On the relevance of Reynolds stresses in resolvent analyses of turbulent wall-bounded flows, J. Fluid Mech. **867**, 969 (2019).

[57] L. I. Abreu, A. Tanarro, A. V. G. Cavalieri, P. Schlatter, R. Vinuesa, A. Hanifi, and D. S. Henningson, Spanwise-coherent hydrodynamic waves around flat plates and airfoils, J. Fluid Mech. **927**, A1 (2021).

[58] R. Pozuelo, A. V. G. Cavalieri, P. Schlatter, and R. Vinuesa, Widestscales in turbulent channels, Phys. Fluids **36**, 025150 (2024).

[59] E. Kim and H. Choi, Space-time characteristics of a compliant wall in a turbulent channel flow, J. Fluid Mech. **756**, 30 (2014).

[60] A. Sano, L. I. Abreu, A. V. G. Cavalieri, and W. R. Wolf, Trailing-edge noise from the scattering of spanwise-coherent structures, Phys. Rev. Fluids **4**, 094602 (2019).

[61] S. Demange, Z. Yuan, S. Jekosch, A. Hanifi, A. V. Cavalieri, E. Sarradj, T. L. Kaiser, and K. Oberleithner, Resolvent model for aeroacoustics of trailing-edge noise, Theor. Comput. Fluid Dyn. **38**, 163 (2024).

[62] J. Borée, Extended proper orthogonal decomposition: A tool to analyse correlated events in turbulent flows, Exp. Fluids **35**, 188 (2003).

[63] F. R. Amaral, A. V. G. Cavalieri, E. Martini, P. Jordan, and A. Towne, Resolvent-based estimation of turbulent channel flow using wall measurements, J. Fluid Mech. **927**, A17 (2021).